CrossMark

J. Fluid Mech. (2019), *vol.* 864, *pp.* 768–806. © Cambridge University Press 2019
doi:10.1017/jfm.2019.45

The cell-free layer in simulated microvascular networks

Peter Balogh[1] **and Prosenjit Bagchi**[1],†

[1]Mechanical and Aerospace Engineering Department, Rutgers, The State University of New Jersey, Piscataway, NJ 08854, USA

(Received 7 June 2018; revised 11 October 2018; accepted 7 January 2019; first published online 11 February 2019)

In the microcirculation, a plasma layer forms near the vessel walls that is free of red blood cells (RBCs). This region, often termed as the cell-free layer (CFL), plays important haemorheological and biophysical roles, and has been the subject of extensive research. Many previous studies have considered the CFL development in single, isolated vessels that are straight tubes or channels, as well as in isolated bifurcations and mergers. In the body, blood vessels are typically winding and sequentially bifurcate into smaller vessels or merge to form larger vessels. Because of this geometric complexity, the CFL *in vivo* is three-dimensional (3D) and asymmetric, unlike in fully developed flow in straight tubes. The three-dimensionality of the CFL as it develops in a vascular network, and the underlying hydrodynamic mechanisms, are not well understood. Using a high-fidelity model of cellular-scale blood flow in microvascular networks with *in vivo*-like topologies, we present a detailed analysis of the fully 3D and asymmetric nature of the CFL in such networks. We show that the CFL significantly varies over different aspects of the networks. Along the vessel lengths, such variations are predominantly non-monotonic, which indicates that the CFL profiles do not simply become more symmetric over the length as they would in straight vessels. We show that vessel tortuosity causes the CFL to become more asymmetric along the length. We specifically identify a curvature-induced migration of the RBCs as the underlying mechanism of increased asymmetry in curved vessels. The vascular bifurcations and mergers are also seen to change the CFL profiles, and in the majority of them the CFL becomes more asymmetric. For most bifurcations, this is generally observed to occur such that the CFL downstream narrows on the side of the vessel nearest the upstream bifurcation, and widens on the other side. The 3D aspects of such behaviour are elucidated. For many bifurcations, a discrepancy exists between the CFL in the daughter vessels, which arises from a disproportionate partitioning between the flow rate and RBC flux. For most mergers, the downstream CFL narrows in the plane of the merger, but widens away from this plane. The dominant mechanism by which such changes occur is identified as the geometric focusing of the two merging streams. To our knowledge, this work provides the first simulation-based analysis of the 3D CFL structure in complex *in vivo*-like microvascular networks, including the hydrodynamic origins of the observed behaviour.

Key words: blood flow, capsule/cell dynamics

† Email address for correspondence: pbagchi@jove.rutgers.edu

https://doi.org/10.1017/jfm.2019.45 Published online by Cambridge University Press

1. Introduction

A well-known characteristic of blood flow in the microcirculation is the formation of a plasma layer adjacent to the vascular walls that is devoid of red blood cells (RBCs). RBCs, the primary cellular component of blood, tend to flow in the central core region of the microvessels. This plasma layer, often referred to as the cell-free layer (CFL), separates the RBC core from the vessel walls (Kim *et al.* 2009*b*). The existence of the CFL has important haemorheological and physiological consequences under both healthy and diseased conditions. Since plasma viscosity is less than haemoglobin viscosity, the CFL provides a means of reducing the apparent viscosity of blood in small vessels. The variation of the CFL thickness with respect to the vessel diameter is related to the decrease in the apparent blood viscosity (Fahraeus–Linqvist effect) and haematocrit (Fahraeus effect) with decreasing vessel diameter (Pries, Secomb & Gaehtgens 1996). As the RBCs occupy the central core region, inactivated platelets and leukocytes marginate towards the vessel walls. The near-wall accumulation of platelets and leukocytes is important in maintaining the body's haemostasis and immune response, respectively. The characteristics of the CFL play a large role in such processes (e.g. Freund 2007; Crowl & Fogelson 2010; Zhao, Shaqfeh & Narsimhan 2012; Fedosov & Gompper 2014). Being situated between the RBC core and the vessel wall, the CFL also affects the wall shear stress, which is sensed by the endothelial cells to trigger diverse pathophysiological functions (e.g. Davies & Tripathi 1993; Smiesko & Johnson 1993; Barbee 2002). In addition, the CFL provides a barrier that inhibits the consumption of nitric oxide (NO), a vasodilator produced in the vascular endothelium (e.g. Rees, Palmer & Moncada 1989; Liao *et al.* 1999). Furthermore, the thickness of the CFL is directly related to the plasma skimming phenomenon, which contributes to a heterogeneous distribution of haematocrit to the daughter branches at a vascular bifurcation (Enden & Popel 1994). In terms of theoretical applications, several low-dimensional models of microvascular blood flow utilize the CFL thickness as an input parameter (e.g. Perkkio & Keskinen 1983; Yan, Acrivos & Weinbaum 1991; Sharan & Popel 2001; Wang & Bassingthwaighte 2003; Secomb & Pries 2013).

Because of its fundamental importance, the CFL has been studied extensively *in vivo* (e.g. Copley & Staple 1962; Soutani *et al.* 1995; Namgung *et al.* 2011), *in vitro* (e.g. Bugliarello & Sevilla 1970; Fenton, Carr & Cokelet 1985; Reinke, Gaehtgens & Johnson 1987) and *in silico* (e.g. Fedosov *et al.* 2010; Yin, Thomas & Zhang 2013). A significant amount of information exists in the literature on the dependence of the CFL thickness on vessel diameter, haematocrit, flow rate and shear rate, among other pertinent quantities. Such works have generally shown that the thickness increases with decreasing haematocrit, increasing flow rate and increasing vessel diameter (Kim *et al.* 2009*b*). In long straight vessels, a number of competing hydrodynamic mechanisms can be identified to play roles in the formation of the CFL (Secomb 2017). Under normal conditions, healthy RBCs are extremely deformable. The deformability results in a migration of the RBCs away from vessel walls, and from regions of higher to lower velocity gradient (Cantat & Misbah 1999; Abkarian, Lartigue & Viallat 2002; Coupier *et al.* 2008; Grandchamp *et al.* 2013; Singh, Li & Sarkar 2014). The centreward migration is countered by the cell–cell interactions (shear-induced diffusion) which tend to disperse the cells over the vessel cross-section (Leighton & Acrivos 1987; Kumar & Graham 2012). For a fully developed and otherwise steady flow in long, straight vessels of circular cross-section, the balance of these competing mechanisms results in the time-averaged CFL being axisymmetric and of constant thickness along the vessel length. Studies on the CFL in such vessels

https://doi.org/10.1017/jfm.2019.45 Published online by Cambridge University Press

have elucidated its characteristics under a diverse range of conditions, including non-axisymmetric entrance profiles (e.g. Fedosov *et al.* 2010; Katanov, Gompper & Fedosov 2015; Oulaid & Zhang 2015).

In the microcirculation, blood vessels form complex networks, and are typically not straight in length. Furthermore, these vessels frequently either bifurcate into smaller vessels or merge to form larger vessels. Owing to these complexities, the CFL as it arises under such circumstances is not expected to be axisymmetric. Rather, the vascular bifurcations, mergers and vessel tortuosity are expected to result in a fully three-dimensional (3D) and highly varying CFL along the length of a vessel in a microvascular network. In the microvasculature of many organs, such as the brain, the blood vessels are of short length so that the flow cannot fully develop. To date, however, these complex aspects of the CFL have been studied either by considering single, isolated vessels, or by considering single bifurcations or mergers. For example, Bloch (1962) performed a comprehensive *in vivo* study of cells flowing in microvascular networks in various organs of different vertebrates. The CFL thickness was observed to be different between the two sides of the vessel, providing evidence to the 3D, asymmetric nature of the CFL *in vivo*. Similar discrepancies in the CFL thickness on either side of individual vessels were noted by Kim *et al.* (2007) in long, unbranched vessels in the rat microvasculature. Studies such as these suggest that CFL asymmetries can arise far away from any disturbances caused by upstream bifurcations or mergers. The hydrodynamics underlying such behaviour, however, remains an open question (Kim *et al.* 2007).

Near bifurcations and mergers, the CFL has been shown to be asymmetric immediately downstream due to the disturbances caused by these structures. The *in vivo* work of Ong, Jain & Kim (2012) studied variations in the CFL near bifurcations, as did the two-dimensional (2D) *in silico* works of Yin *et al.* (2013) and Ye, Ju & Kim (2016). These studies reported a thinner CFL on the side of the daughter vessel that was closest to the bifurcation. The *in vivo* work of Namgung & Kim (2014) studied the change in the CFL caused by two merging vessels, and observed the downstream CFL to be asymmetric. They further noted that the asymmetry increased with increasing discrepancy in the flow contributions from each feeding vessel, which apparently alludes to a hydrodynamic mechanism for the CFL development under such geometries.

The existing knowledge of the CFL *in vivo*, however, has been based on characterizing it as a 2D projection onto the image plane. As such, the reported asymmetry in the CFL in the aforementioned studies is based on the thickness values on either side of a vessel as observed in the 2D projection. As noted before, because of the presence of frequent bifurcations, mergers and vessel tortuosity, the asymmetry of the CFL is expected to be fully 3D in nature and to evolve within the network in a more complex manner than what can be captured by the 2D projection. The full 3D nature of the CFL asymmetry and the underlying hydrodynamic mechanisms by which it arises are not well understood, and are thus the subject of the present study.

We have recently developed a high-fidelity, 3D computational approach to model flow of many deformable RBCs in complex microvascular networks resembling an *in vivo*-like architecture, as in figure 1 (Balogh & Bagchi 2017*a*,*b*, 2018). Using the data from our previously reported simulations (Balogh & Bagchi 2017*b*), here we present a detailed study on the fully 3D nature of the CFL as it arises in such *in vivo*-like geometries. Because of the geometric complexity of vascular networks, a 2D projection to extract the CFL is not sufficient. As such, we first describe a method to obtain the full 3D CFL from the simulation data in a consistent way

https://doi.org/10.1017/jfm.2019.45 Published online by Cambridge University Press

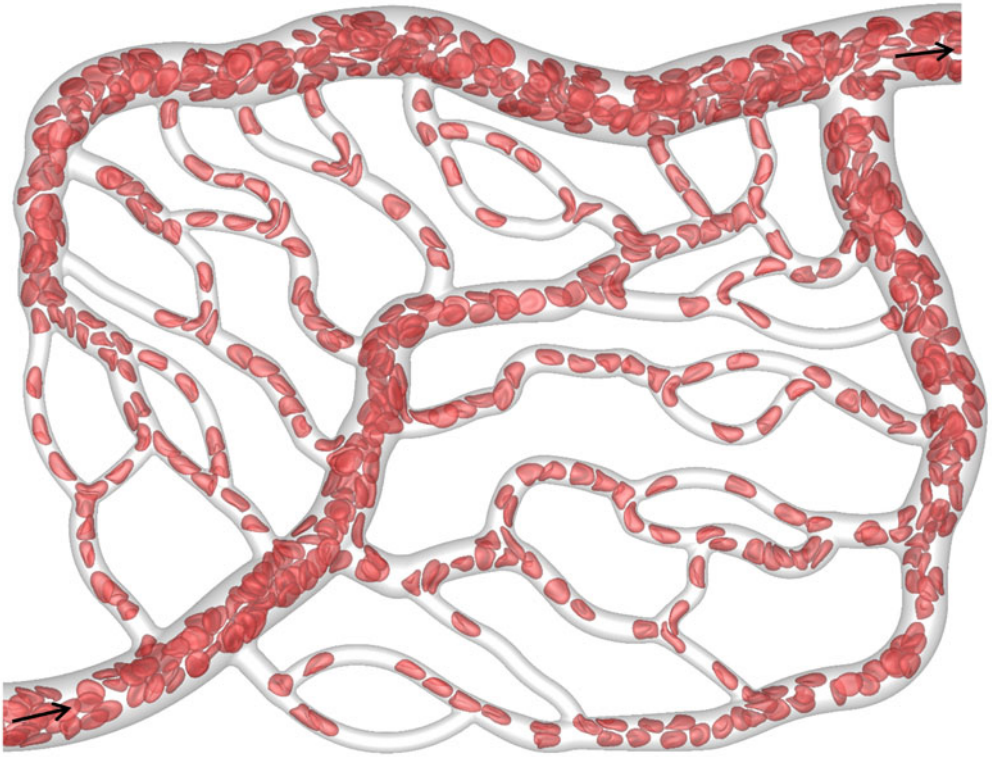


FIGURE 1. (Colour online) An instant in the simulation of RBCs flowing in one of the three microvascular networks. Arrows indicate flow directions at the network inlet and outlet.

for different vessels under diverse haemodynamic conditions. Next, we quantify the 3D asymmetry in the CFL, and identify the underlying hydrodynamic mechanisms that cause such asymmetry in various segments of vascular networks, namely, vessel segments, bifurcations and mergers. We show that vessel tortuosity can result in an asymmetric CFL because of the presence of a curvature-induced migration of the RBCs. We further show that the vascular bifurcations can increase the asymmetry in the CFL, and we establish a hydrodynamic basis for the discrepancy in the CFL in the daughter vessels downstream of the bifurcations. Similarly, we show that the CFL asymmetry increases over the vascular mergers, and we identify the geometric focusing effect as a dominant underlying mechanism.

2. Overview of simulations

The simulation details have been given in Balogh & Bagchi (2017*b*), and the underlying numerical methodology was described in Balogh & Bagchi (2017*a*). Only the essential information is provided below.

Three different microvascular networks were designed following *in vivo* images and data (Lipowsky, Kovalcheck & Zweifach 1978; Fung 1996; Zakrzewicz, Secomb & Pries 2002; Cassot *et al.* 2006; Benedict *et al.* 2011). An image of one network is provided in figure 1 showing the distribution of the deformed RBCs at one time instant. The additional networks are provided in the supplementary material

https://doi.org/10.1017/jfm.2019.45 Published online by Cambridge University Press

available at https://doi.org/10.1017/jfm.2019.45. As is evident, the designed networks are geometrically complex, and comprise multiple bifurcations, mergers and winding vessels, resembling topological structures commonly observed *in vivo*. Collectively, these contain 138 vessels, with diameters ranging from 6 to 24 μm and lengths ranging from 25 to 165 μm. Also, there are 45 bifurcations and 45 mergers. For each network, four different simulations were performed using different boundary conditions, resulting in 12 total simulations. A pressure difference between the main inlet and outlet was used to drive the flow for nine simulations, with values in the range 0.3–1.0 Pa μm^{-1}. The pressures applied at the inlet and outlet faces were chosen so that the average pressure loss per length over the network equalled the minimum, mean or maximum *in vivo* values given in Fung (1996). For the other three simulations the flow rate in the main feeding artery was specified, with values of $(2\text{–}4.6) \times 10^{-13}$ m^3 s^{-1}. The exact values of the boundary parameters and additional discussion on the pressure versus flow rate boundary conditions are given in Balogh & Bagchi (2017*b*, 2018). For each network, an initializing simulation is performed where the haematocrit in the main feeding artery is maintained at approximately 30 %. The RBCs are initially distributed randomly throughout the network, and their undeformed shape is taken as the experimentally observed biconcave discocyte (Fung 1996). Following this initialization, the RBC distribution is allowed to develop naturally and evolve throughout the networks. Once a quasi-steady state is reached, data are stored every 0.5 ms. For each of the 12 simulations, data corresponding to 1400 time instants are used for analysis. For the simulations performed to reach a quasi-steady state, the duration of this was such that each RBC passed through the network a few times. It was observed that this was sufficient to remove any effects of the initial placement and orientation of the cells. Quantitatively, we monitored the time signals for quantities such as vessel flow rates, haematocrit and pressure drop (Balogh & Bagchi 2017*b*). After each RBC passed through the network a few times, this generally corresponded to the time at which the oscillations in these signals were in a quasi-steady/repeating state.

Some limitations of the simulated networks in comparison to *in vivo* conditions may be noted. First, the vessel walls are assumed non-deformable. However, the typical time associated with the vasomotion is much larger than the RBC transit time. Second, most vessels *in vivo* have non-circular cross-sections while here they are modelled as circular. Furthermore, the inner wall of the vessels *in vivo* is covered with endothelial cells. The presence of these cells and the glycocalyx layer on their surface are not modelled. Additionally, white blood cells and platelets are not considered.

The numerical methodology used to perform the simulations is based on the immersed boundary method (IBM), implemented in the context of a finite-volume/spectral fluid flow solver (Balogh & Bagchi 2017*a*). Using this, the 3D flow field within the highly complex network architectures is modelled, while simultaneously resolving the large deformation and 3D dynamics of each individual RBC with high fidelity. At the foundation of the approach, the equations governing the fluid flow are

$$\rho \frac{\partial \boldsymbol{u}}{\partial t} = -\boldsymbol{\nabla} p + \boldsymbol{\nabla} \cdot \mu[\boldsymbol{\nabla u} + \boldsymbol{\nabla u}^{\mathrm{T}}], \quad \boldsymbol{\nabla} \cdot \boldsymbol{u} = 0, \tag{2.1}$$

which are the unsteady Stokes equations for a variable-viscosity, constant-density fluid, and the conservation of mass, respectively. The modelled network is built using computer-aided design (CAD) software, and vessel walls are discretized using a triangulated surface mesh. The network is immersed within a rectangular Eulerian mesh of approximately 8×10^7 grid points in the shape of a box. Both the vascular

https://doi.org/10.1017/jfm.2019.45 Published online by Cambridge University Press

walls and the cells are immersed into this domain, and their presence is simulated when solving the governing equations using two different IBMs. The flow equations are solved in this domain with a staggered arrangement of the primitive variables, and spatial derivatives are evaluated using second-order differencing. The time integration is performed by means of a projection method, where an advection–diffusion equation is solved using an alternating direction implicit (ADI) scheme to enforce the conservation of momentum, and a Poisson-type equation is solved using a spectral-based approach to enforce the conservation of mass.

For the vascular walls, a sharp-interface ghost node method is used which essentially modifies the governing system of equations with constraints on the velocity field. These are enforced at Eulerian grid points immediately outside the vessels such that a no-slip condition is achieved at the walls. For the deformable cells, a continuous forcing IBM, namely, a front-tracking method, is used. Each RBC is modelled as a viscous haemoglobin drop surrounded by a zero-thickness hyperelastic membrane. The strain energy function of Skalak *et al.* (1973) is used for the shearing deformation and area dilation of the membrane, while Helfrich's formulation for bending energy (Zong-can & Helfrich 1989) is used to model the bending resistance. The viscosity of the haemoglobin is considered to be five times that of the plasma (Fung 1993). The continuous forcing IBM couples the stresses in the RBC membrane to the bulk fluid via a body force-like term added to the flow equations. The surface of each cell is discretized by a Lagrangian mesh of 5120 Delaunay triangles, and a finite-element method is used to compute the membrane stress generated as a result of shear deformation and area dilatation. The net membrane force is distributed to the surrounding fluid from each of the Lagrangian nodes using the 3D delta function. The discontinuity in viscosity across the cell membrane is spread over a finite region of the Eulerian domain using the 3D delta function in a similar manner to the membrane force. As the governing equations are solved from one time step to the next, each cell membrane is advected with the velocity obtained by interpolating from the surrounding fluid using the same delta function, giving the new location and shape.

2.1. *Cell-free layer calculation*

A fundamental component to the present analysis is the means by which the CFL is determined. The methodologies used to determine the CFL in previous experimental works have typically involved constructing some form of an RBC core used in conjunction with the location of the vessel walls. Among these works, however, different approaches have been taken. Earlier *in vivo* works (e.g. Bloch 1962; Tateishi *et al.* 1994; Soutani *et al.* 1995; Maeda *et al.* 1996) and *in vitro* works (e.g. Bugliarello & Sevilla 1970; Reinke *et al.* 1987) determined the CFL thickness by visual observation and analysis of video images. More recently, *in vivo* works such as Kim *et al.* (2006) or Ong *et al.* (2011) have developed automated image analysis methods to digitally construct the RBC core and cell-free regions at individual instants in time. Specifically, the method developed in Kim *et al.* (2006) constructed the core and cell-free regions as a binary image which assumed a continuous core between any plasma gaps separating individual RBCs along the length. Ong *et al.* (2011) improved on this with a greyscale image-based method that provides increased accuracy in faint areas.

Somewhat similar approaches have been adopted in previous computational modelling. Fedosov *et al.* (2010) simulated RBCs flowing in a straight tube using a

https://doi.org/10.1017/jfm.2019.45 Published online by Cambridge University Press

dissipative particle dynamics method, and constructed an RBC core by projecting the cell outline along the vessel length onto a 2D plane in a manner similar to Kim *et al.* (2006). Yin & Zhang (2012), for their 2D lattice-Boltzmann simulations, determined the CFL as the average of the closest cell-wall distances between each side of the vessel. For the simulations in Yin *et al.* (2013), the CFL thickness was determined as the boundary of the region near the wall that is occupied by 2.5 % of the total RBC volume, while Ye *et al.* (2016) used an occurrence frequency distribution of CFL values at locations in the modelled vessel.

Evidently, a wide variety of approaches have been used to determine the CFL in prior works. In the present work, because of the geometric complexity of the microvascular networks, and the resulting effect on the formation of the RBC core, a 2D projection of the core to determine the CFL would not be sufficient. Furthermore, the distribution of the RBCs across a network is highly heterogeneous, and constantly changes over time. As such, the CFL distribution across the network is heterogeneous and time-dependent. Owing to the heterogeneity of the RBC distribution, some vessels are constantly filled with cells, while some have intermittent flows of cells. In many vessels, especially in the small capillaries, there are instants when only one or two cells are flowing through a vessel, or cells flow through a vessel in a manner in which there are plasma gaps in between the cells along the vessel length. A methodology is thus needed for the present work to accurately compute the 3D time-dependent CFL under these different flow conditions. As such, the procedure developed for calculation of the CFL in the present work is given in appendix A. Also included is a comparison with *in vivo* values from the literature.

3. Results and discussion

3.1. *Three-dimensionality of cell-free layer*

We first describe the general 3D nature of the CFL as predicted in the simulated networks. The analysis of the underlying mechanisms is presented in the subsequent sections.

The three-dimensionality is first described using a representative vessel as shown in figure 2(*a*). The time-dependent profiles of the RBC core over the vessel cross-sections are shown in figure 2(*b*) at four different locations along the vessel length, along with the time-averaged profiles superimposed. As figure 2(*b*) suggests, the time-dependent profiles at any cross-section are highly non-circular, significantly distinct at each instant, and deviate significantly from the time-averaged profiles. Also, at any time instant the cross-sectional profiles are different at different locations. To further demonstrate the 3D and non-circular nature of the CFL, we consider its variation along the vessel length but at two diametrically opposite sides, L and R, as shown in figure 2(*a*). The CFL thicknesses along these sides are denoted as $\delta_L(s, t)$ and $\delta_R(s, t)$, respectively, and both time-dependent and time-averaged results are presented in figure 2(*c*,*d*). While these quantities themselves give the thickness as in a 2D projection approach, when taken in conjunction with the cross-sectional profiles these collectively paint a 3D picture of the CFL. Figure 2(*b–d*) shows that both the time-dependent and time-averaged CFL vary significantly along the vessel length. The differences between δ_L and δ_R are significant, for both the time-dependent and time-averaged results, serving as evidence of the asymmetric nature of the CFL. While both time-averaged δ_L and δ_R vary along the length, δ_L shows a greater variation than δ_R. Furthermore, δ_L generally increases along the vessel length while δ_R does not have a net change between the vessel entrance and exit. The root mean square

https://doi.org/10.1017/jfm.2019.45 Published online by Cambridge University Press

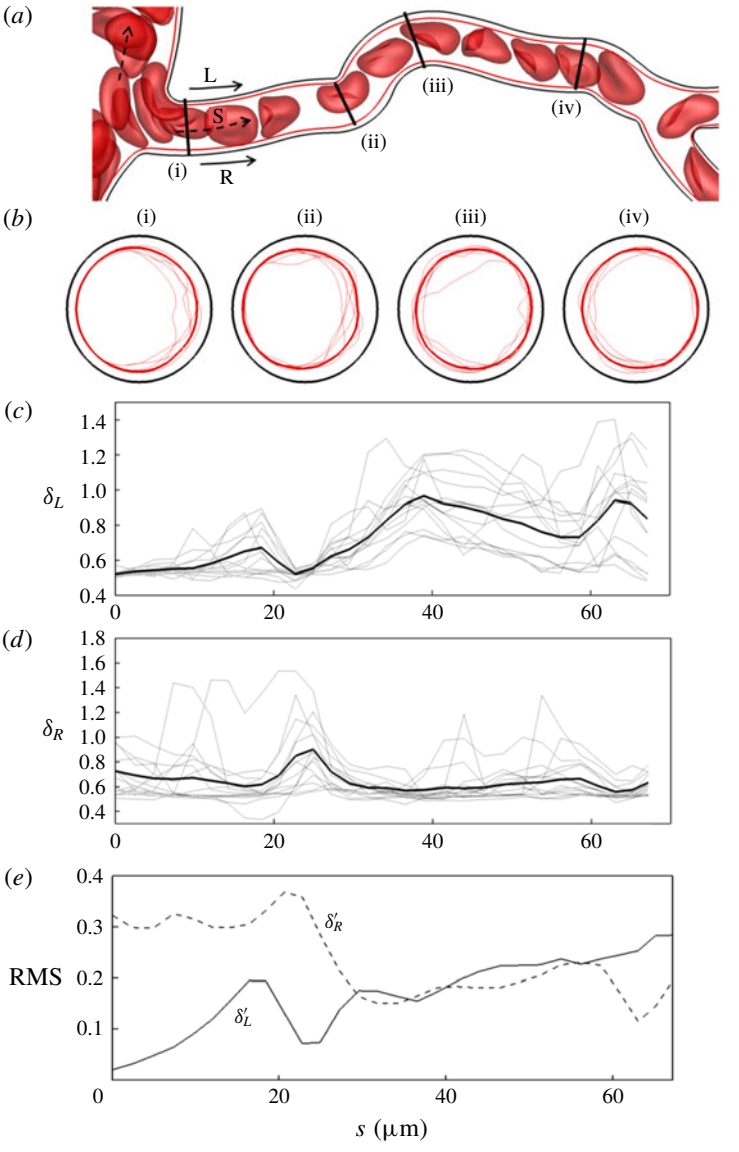


FIGURE 2. (Colour online) (*a*) An instant of RBCs flowing in an example vessel in one of the simulated networks. Here R and L denote the right and left sides in the plane of the figure, respectively. (*b*) The time-averaged (thick line) and instantaneous (thin lines; several instants are shown) RBC core over the vessel cross-section at four different axial locations. (*c*,*d*) Time-averaged (thick line) and instantaneous (thin lines) CFL thickness along L and R, respectively. (*e*) Root mean square (r.m.s.) of temporal fluctuations in the CFL thickness along L and R.

(r.m.s.) values of the temporal fluctuations of δ_L and δ_R scaled by the time-averaged thickness at each location along the length are shown in figure 2(*e*). Interestingly, temporal fluctuations in δ_L generally increase along the vessel length, while those in δ_R decrease.

https://doi.org/10.1017/jfm.2019.45 Published online by Cambridge University Press

Figure 2 generally shows that not only is the time-dependent CFL highly 3D and asymmetric, but the time-averaged CFL is as well. In contrast, for a fully developed flow in straight tubes of circular cross-section, though the time-dependent CFL is generally 3D, the time-averaged CFL is axisymmetric. Thus in the present work we primarily focus on studying the three-dimensionality in the time-averaged CFL as it arises in complex networks.

To quantify the 3D and asymmetric nature of the time-averaged CFL, first we consider an asymmetry parameter defined as

$$\varepsilon(s) = \frac{\overline{\delta}_{max}(s)}{\overline{\delta}_{min}(s)}, \tag{3.1}$$

where $\overline{\delta}_{max}(s)$ and $\overline{\delta}_{min}(s)$ are the maximum and minimum values, respectively, of the time-averaged CFL thickness over the vessel cross-section ($0 \leqslant \theta < 2\pi$) at any location s along the vessel length. This gives a value of one for a symmetric profile, and values greater than one for increasing asymmetry. The $\varepsilon(s)$ value is plotted in figure 3(*a*) for a few representative vessels with length-to-diameter ratio in the range of 10–15. Several important observations are made here. First, this shows that, even for relatively long vessels, the time-averaged CFL does not become axisymmetric over the length. While for some vessels the profile becomes more symmetric near the end, for others it becomes more asymmetric. Second, while there may be a net increase or decrease in ε between the inlet and exit of a vessel, there is a significant fluctuation along the vessel length. This often results in the extremum of ε occurring at locations in the middle of the vessels rather than at the inlet and exit. In vessels where the extremum of ε does occur at the inlet and outlet, ε does not typically change monotonically along the length but rather fluctuates significantly as well. Even when ε is nearly the same at the inlet and outlet, in between, fluctuations of large magnitudes are observed. These results are in contrast to what would happen in a straight tube, where any CFL asymmetry at the inlet would monotonically decrease over the vessel length.

To quantify the CFL asymmetry ε for all vessels in the network, we compute the difference between ε at the beginning and end of each vessel, i.e. $\varepsilon|_{s=L} - \varepsilon|_{s=0}$, and plot this with respect to the cumulative change in ε over the length defined as $\Delta\varepsilon = \sum_i |\mathrm{d}\varepsilon(s_i)|$. Here, $\Delta\varepsilon$ is evaluated by dividing each vessel into N finite segments, each given by the index i. The relationship between these quantities is presented in figure 3(*b*). If ε were to change monotonically over the length, then $\Delta\varepsilon$ would equal the magnitude of $\varepsilon|_{s=L} - \varepsilon|_{s=0}$. This relationship is given by two straight lines in figure 3(*b*): the line $\Delta\varepsilon = -(\varepsilon|_{s=L} - \varepsilon|_{s=0})$ corresponds to a straight tube, where an asymmetric CFL profile at the vessel entrance monotonically shifts towards a symmetric one with increasing axial distance. In contrast, the line $\Delta\varepsilon = +(\varepsilon|_{s=L} - \varepsilon|_{s=0})$ means the asymmetry at the inlet monotonically increases along the length. As figure 3(*b*) shows, most data points from the simulations lie above the lines, i.e. $\Delta\varepsilon > |(\varepsilon|_{s=L} - \varepsilon|_{s=0})|$, meaning that the CFL does not change monotonically along the vessel length. Even for vessels in which $\varepsilon|_{s=L} - \varepsilon|_{s=0} \approx 0$, $\Delta\varepsilon$ may have large values. Furthermore, of the points that do nearly fall on the lines, some of them are on the $\Delta\varepsilon = +(\varepsilon|_{s=L} - \varepsilon|_{s=0})$ line, which means the asymmetry at the inlet monotonically increases with length. Overall, figure 3(*b*) suggests that, while there may be a net increase or decrease in ε between the inlet and outlet, the evolution of ε over the length is much more complex, and, in most vessels, the time-averaged CFL profile varies significantly and non-monotonically along the vessel length.

https://doi.org/10.1017/jfm.2019.45 Published online by Cambridge University Press

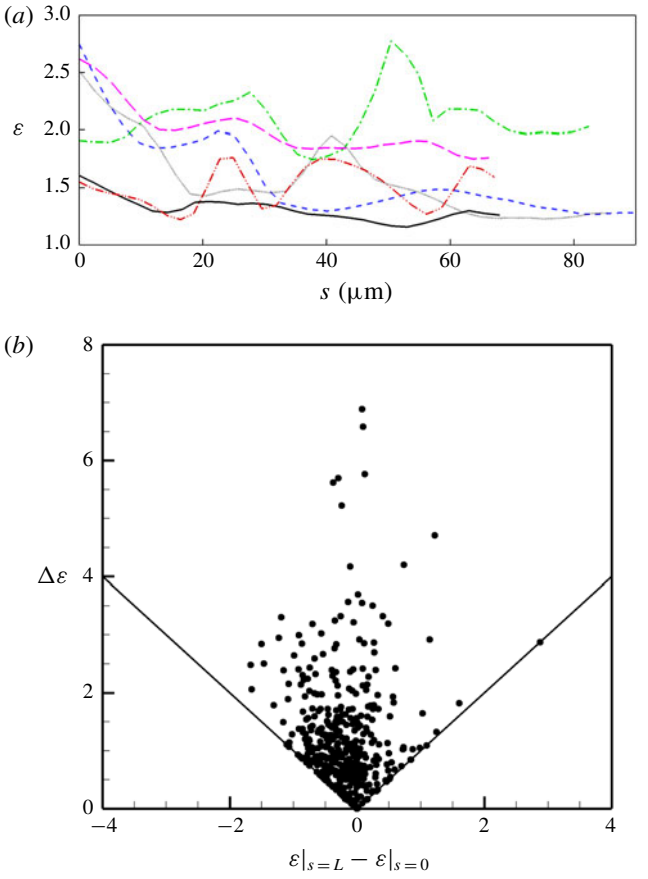


FIGURE 3. (Colour online) (*a*) The CFL asymmetry parameter ε along the length for several representative vessels in the network. (*b*) The change in asymmetry, $\varepsilon|_{s=L} - \varepsilon|_{s=0}$, between vessel inlet and outlet versus the cumulative change $\Delta\varepsilon$ over the entire length, for all vessels (data points). The straight lines correspond to a monotonic change in ε over the length.

The number of segments N used in the above analysis typically corresponded to a spacing of roughly one-quarter of the vessel diameter. This was found to be fine enough to capture variations of the RBC core along vessel lengths, and resolve the curvature of the vessel centreline. Since these variations are adequately captured, the resolution is deemed sufficient.

Additional quantification of the 3D, non-symmetric nature of the time-averaged CFL is made by considering the angular locations on the vessel cross-section where the maximum and minimum thickness values occur, denoted by the angles $\theta_{\delta=\delta\,max}$ and $\theta_{\delta=\delta\,min}$, respectively. As noted in appendix A, θ is defined using the vessel centreline as the origin and looking downstream in the flow direction. Here, $\theta = 0$ is located on the plane passing through the vessel centreline at the location on the perimeter closest to the upstream bifurcation (see figure 21 in appendix A). Figure 4 presents the variations in $\theta_{\delta=\delta\,max}$ and $\theta_{\delta=\delta\,min}$ over the length of the same representative vessels as considered in figure 3(*a*). When plotting these values along the vessel length, the sign of θ was chosen so as to result in a smooth curve without discontinuities.

https://doi.org/10.1017/jfm.2019.45 Published online by Cambridge University Press

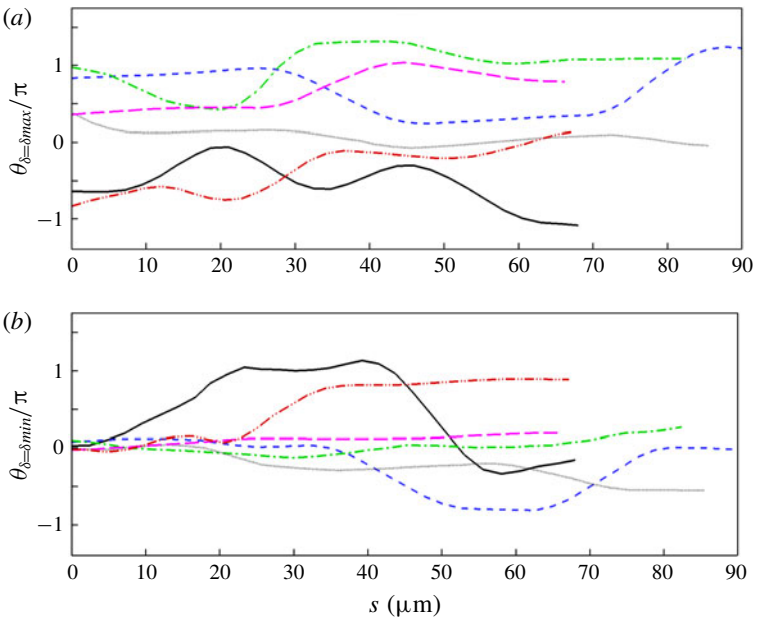


FIGURE 4. (Colour online) Axial variation of the angular locations on the vessel cross-section where the maximum and minimum time-averaged CFL thicknesses occur, denoted by the angles $\theta_{\delta=\delta\,max}$ and $\theta_{\delta=\delta\,min}$, respectively. Results are shown for the same six vessels as in figure 3(*a*), with angles given as fractions of π.

Figure 4 shows that there are significant variations in $\theta_{\delta=\delta\,max}$ and $\theta_{\delta=\delta\,min}$ along the vessel length. Another interesting observation in figure 4 is that $\theta_{\delta=\delta\,min} \approx 0$ at vessel entrances, meaning that the location of the minimum CFL thickness occurs on the side of the vessel that is closest to the upstream bifurcation. In contrast, $\theta_{\delta=\delta\,max}$ at vessel entrances is such that the maximum thickness is observed to occur at any location over the perimeter. Additional analysis of $\theta_{\delta=\delta\,max}$ and $\theta_{\delta=\delta\,min}$ and the underlying cellular-scale mechanisms will be considered in later sections. It is noted that, while these examples utilize vessels on the arterial side, similar fluctuations and variations with vessel length were observed in post-capillary venules as well.

Together, figures 2–4 demonstrate the highly complex, 3D and asymmetric nature of the time-averaged CFL in the vessels comprising the network. Next, we identify and analyse the mechanisms that give rise to such complexity. These mechanisms are discussed as they arise in three different facets of the networks, namely, along the vessel lengths, and over the bifurcations and the mergers.

3.2. *Mechanism causing cell-free layer variations along vessel length*

In this section, we identify a primary mechanism causing the axial variations in the time-averaged CFL. In general, the CFL at the entrance to a vessel in the networks is asymmetric due to the presence of the upstream bifurcation or merger. If the vessel were straight, the asymmetric CFL at the entrance would gradually shift towards a symmetric profile with increasing axial distance. This has been shown *in vivo* in such works as Ong *et al.* (2012), and *in silico* in Katanov *et al.* (2015), among others. Most

https://doi.org/10.1017/jfm.2019.45 Published online by Cambridge University Press

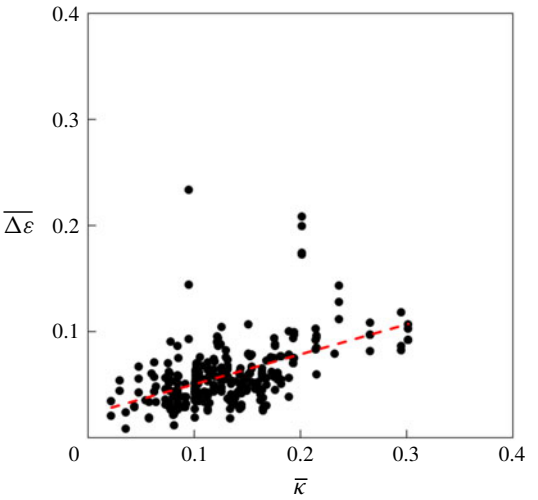


FIGURE 5. (Colour online) Effect of vessel tortuosity. The mean absolute change in asymmetry, $\overline{\Delta\varepsilon}$, is presented as a function of the mean absolute curvature, $\overline{\kappa}$, for every vessel. The red dashed line is a linear regression of the data.

vessels in the networks are, however, winding. We find that vessel tortuosity results in the increased asymmetry of the CFL along the length, as discussed below.

To quantify the effect of vessel tortuosity, we consider the curvature of the vessel centreline, defined as $\kappa(s) = R/r(s)$, where $r(s)$ is the radius of curvature of the vessel centreline at an axial location s, and R is the vessel radius. As a measure of tortuosity, the mean absolute curvature is defined as

$$\overline{\kappa} = \frac{\sum_{i=1}^{N} |\kappa(s_i)|}{N}, \tag{3.2}$$

which is computed by dividing each vessel into N finite segments, as previously described. In addition, as a measure of the axial variation of the CFL, we define the mean absolute change in the asymmetry parameter ε as

$$\overline{\Delta\varepsilon} = \frac{\sum_{i=1}^{N} |\mathrm{d}\varepsilon(s_i)|}{N}. \tag{3.3}$$

In figure 5, we plot $\overline{\Delta\varepsilon}$ as a function of $\overline{\kappa}$ for all vessels. This figure shows that $\overline{\Delta\varepsilon}$ generally increases with increasing $\overline{\kappa}$, which implies that the CFL asymmetry is higher in winding vessels. The plot, however, also shows a noticeable scatter, which will be discussed later.

It is noted that $\Delta\varepsilon$ is the change in CFL asymmetry, not the asymmetry itself. The trend that $\Delta\varepsilon \to 0$ as $\kappa \to 0$ as in figure 5 means that, for a relatively straight vessel, the change in the CFL asymmetry over the vessel length tends to be very small. This is expected, for example, because the CFL profile can be asymmetric at the inlet to a

https://doi.org/10.1017/jfm.2019.45 Published online by Cambridge University Press

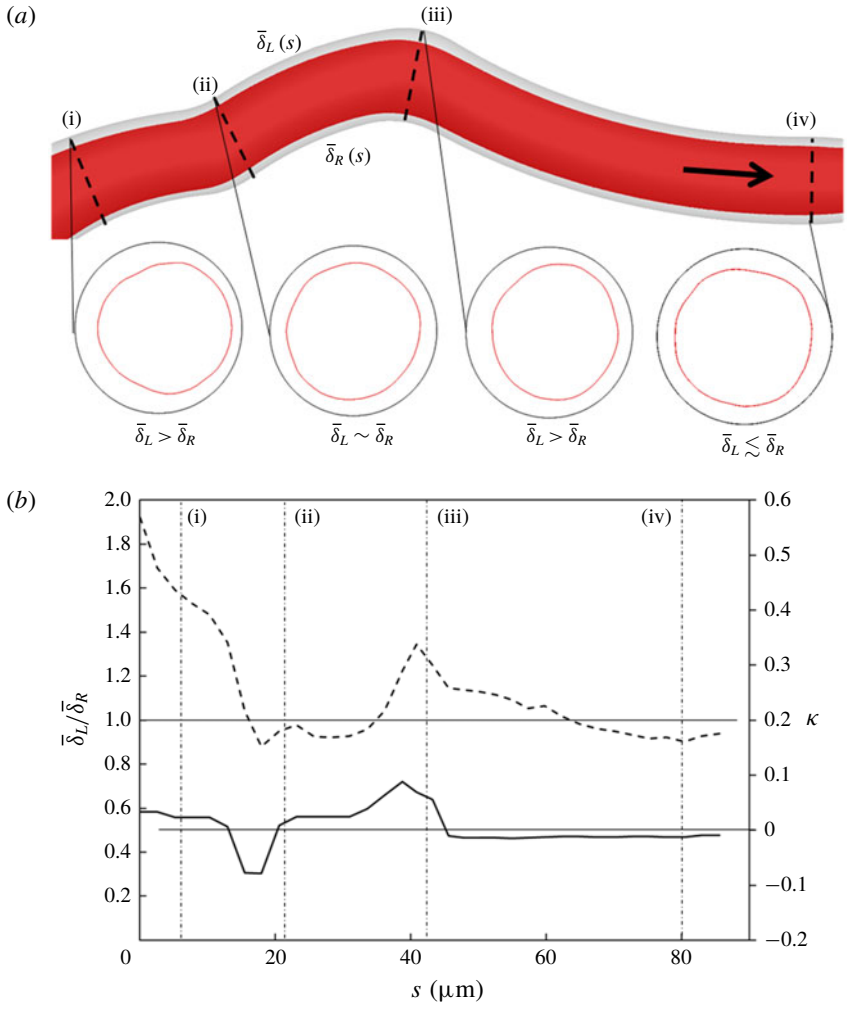


FIGURE 6. (Colour online) Effect of vessel centreline curvature on the time-averaged CFL profile. (*a*) A representative vessel showing the time-averaged RBC core and the cross-sectional profiles at four axial locations marked as (i)–(iv). Here $\overline{\delta_L}(s)$ and $\overline{\delta_R}(s)$ are the CFL thicknesses along the left and right sides of the vessel, respectively, in the plane of the figure looking in the flow direction (arrow). (*b*) Plots of $\overline{\delta_L}/\overline{\delta_R}$ (dashed line, left axis) and centreline curvature κ (solid line, right axis) along the vessel length.

vessel, but if the vessel has a small curvature the change in the CFL asymmetry will be small.

Having established that the CFL asymmetry generally increases with increasing vessel tortuosity, we now consider how the CFL profile at an axial location is affected by the centreline curvature at that location. This is illustrated in figure 6 using a representative vessel from one network. The time-averaged RBC core along the vessel length is shown, along with the cross-sectional profiles at four different axial locations. The centreline curvature, and the ratio $\overline{\delta_L}(s)/\overline{\delta_R}(s)$, which is the ratio of the time-averaged CFL thickness on diametrically opposite sides of the vessel in the plane of the figure, are plotted in figure 6(*b*). In the present orientation, a

https://doi.org/10.1017/jfm.2019.45 Published online by Cambridge University Press

negative curvature occurs when a vessel bends to the left looking downstream in the flow direction, and *vice versa*. At location (i), which is near the entrance, the profile is asymmetric ($\overline{\delta_L} > \overline{\delta_R}$), due to the influence of the upstream bifurcation. As the flow naturally develops along the axial direction, the CFL becomes symmetric at location (ii). This symmetric profile however becomes asymmetric again at location (iii) where $\overline{\delta_L} > \overline{\delta_R}$. Beyond location (iii), the RBC core gradually shifts towards the left side of the vessel, and at location (iv), $\overline{\delta_L} \lesssim \overline{\delta_R}$. Hence, when the vessel bends to the right, the RBC core also shifts to the right, resulting in a thinner CFL on the right side but a thicker CFL on the left. Conversely, when the vessel bends to the left, the RBC core shifts to the left, resulting in a thinner CFL on the left side of the vessel and a thicker CFL on the right.

What these results imply is the presence of a curvature-induced migration of the RBCs. To further illustrate this phenomenon, we simulate the flow of an isolated RBC in a semicircular tube as shown in figure 7. The flow is driven by a pressure difference between the inlet and outlet, and the cell is initially placed symmetrically on the centreline of the tube. If the tube were straight, the cell would flow along the centreline. However, for the curved tube, the predicted trajectory shows that the cell deviates from the centreline and migrates towards the side of the vessel that has higher curvature. The hydrodynamic origin of such migration is as follows. In the absence of inertia, as is the case for the present work, no secondary flow exists in a bending vessel of constant curvature. The pressure is then constant over each subsequent cross-section, and varies only along the axial direction. As such, the axial pressure gradient is larger for a streamline that is closer to the side of the vessel with shorter length than the one that is closer to the other side. This causes the maximum velocity of the undisturbed flow to be shifted towards the side of the vessel with smaller arclength, as predicted in figure 7. This shift in the velocity profile in the absence of inertia has been noted in a number of previous works (e.g. Murata, Miyake & Inaba 1976; Chadwick 1985; Wang & Bassingthwaighte 2003; Verkaik *et al.* 2009). Since a deformable cell tends to migrate in the direction of decreasing velocity gradient (e.g. Coupier *et al.* 2008), the shifted velocity profile causes the cell to migrate away from the vessel centreline and towards the side of the vessel with the shorter arclength.

It should be noted that the mechanism presented in figure 7 is not the only mechanism leading to the CFL formation in a curved vessel. The equilibrium CFL in a suspension of cells is established under the balance of multiple forces. In particular, for a straight vessel, the two dominant forces are the hydrodynamic lift and the shear-induced diffusion. What figure 7 suggests is that, in a vessel such as this, the lift force that would be experienced in a straight vessel is modified by the vessel curvature. Similar to the hydrodynamic lift that acts on a single cell in a straight vessel, this curvature-induced migration caused by the modified lift force also acts on a single cell. Therefore, when a suspension of cells flows in a curved vessel, the CFL is established under the balance of the curvature-modified hydrodynamic lift and shear-induced diffusion due to cell–cell interactions. Just as the hydrodynamic lift in a straight tube can be explained in terms of the velocity profile of the undisturbed flow, so can the curvature-induced migration be explained using the undisturbed velocity profile.

The mechanism of curvature-induced migration given by the example in figure 7 is generic. We have performed additional simulations by varying the tube diameter, radius of curvature and flow rate. The resulting RBC shape (e.g. parachute versus slipper shapes) depends on such parameters, but a migration off-centre is always

https://doi.org/10.1017/jfm.2019.45 Published online by Cambridge University Press

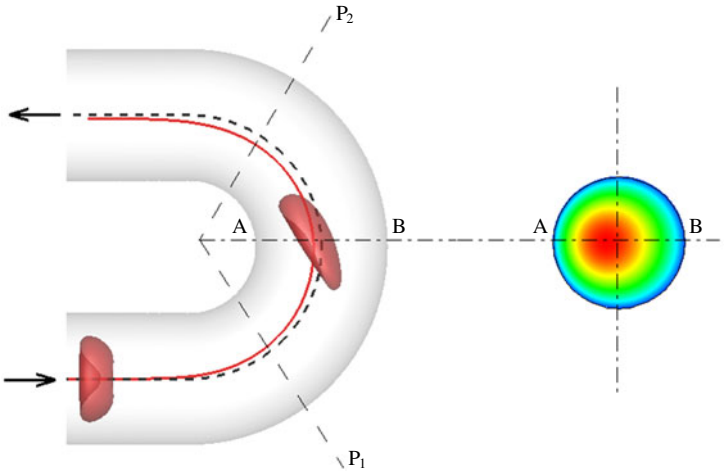


FIGURE 7. (Colour online) Curvature-induced migration of an RBC. The motion of an RBC in a semicircular tube is simulated in the absence of inertia. The flow is driven by constant pressures over the cross-sections at the inlet and outlet. The vessel centreline is given by the dashed line, and the trajectory of the RBC centre of mass is given by the continuous line. The cell trajectory deviates from the centreline and towards the side of the vessel with the shorter arclength. The contour on the right shows the velocity magnitude of the undisturbed flow in cross-section A–B looking in the flow direction. The maximum velocity is shifted towards A.

observed. The example considered in figure 7 provides a good framework for studying not only the curvature-induced migration of a single cell, but also how the geometry of a curved vessel modulates the lift–diffusion balance leading to the CFL for a cell suspension. For such a case, the precise means by which this balance is modulated by the geometry will depend on many factors. These probably include haematocrit profile at the entrance to the curved vessel, vessel radius, vessel curvature, changes in vessel curvature along the length, vessel haematocrit and flow rate. At present we have identified this mechanism underlying increased CFL asymmetry in curved vessels within complex networks. A more detailed parametric/benchmark study could be used to delve further into the underlying principles using an idealized geometry such as a U-shaped tube, although this is beyond the scope of the present work.

When considering the effect of the curvature-induced migration on the CFL profile in a curved vessel, this indicates that the local CFL thickness would be smaller on the side of the vessel with a higher curvature, and *vice versa*. Hence, the vessel curvature causes increased asymmetry of the CFL. If the vessel bends more often, the cross-sectional CFL profile would shift from one side to the other along the length.

In addition to the curvature itself, the rate of change in curvature also locally enhances the CFL asymmetry. In figure 6(*b*) it can be seen that κ drops abruptly near profile (ii) and increases abruptly near profile (iii), which corresponds to the locations where $\delta_{\overline{L}}/\delta_{\overline{R}}$ most abruptly decreases and increases, respectively. Since the fluid velocity would be more skewed with increasing curvature, when the curvature changes over a small length it can induce an additional shift in the RBC core and enhance the asymmetry in the CFL. Such behaviour is in fact observed in the simple example in figure 7, where the most abrupt changes to the RBC trajectory occur at the two locations where the vessel curvature changes (i.e. at the location where the vessel changes from straight to curved, and then back from curved to straight).

https://doi.org/10.1017/jfm.2019.45 Published online by Cambridge University Press

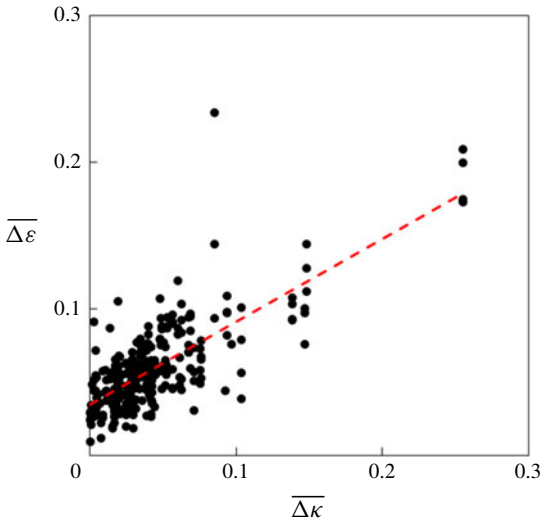


FIGURE 8. (Colour online) Influence of change in curvature on the CFL asymmetry. Plotted here is the cumulative change in centreline curvature versus the cumulative change in ε for each vessel in the network. The red dashed line is a linear regression of the data.

To quantify the effect of curvature change, we define a mean absolute change in vessel curvature as

$$\overline{\Delta\kappa} = \frac{\sum_{i=1}^{N} |\mathrm{d}\kappa(s_i)|}{N}, \tag{3.4}$$

where $\mathrm{d}\kappa(s_i)$ is the change in curvature in segment i along the length. The mean absolute change in the CFL asymmetry, $\overline{\Delta\varepsilon}$, is plotted against $\overline{\Delta\kappa}$ in figure 8. The general trend in the data suggests that $\overline{\Delta\varepsilon}$ increases with increasing $\overline{\Delta\kappa}$, and implies that curvature fluctuations lead to CFL asymmetry variations.

With regard to the data scatter in figures 5 and 8, it should be noted that, in a microvascular network, the haemodynamic quantities such as flow rate and haematocrit are highly heterogeneous. As such, the CFL and its characteristics, such as the asymmetry, are also widely varying between different vessels, resulting in data scatter. Additionally, the mean absolute change in asymmetry can be relatively small for some vessels with larger mean absolute curvature. This occurs in vessels where the RBC core at the entrance is skewed towards the side with higher curvature. Since the profile is already shifted towards the side favoured by curvature, the average change in the CFL profile over the vessel length would be small. Changes to the CFL due to changes in curvature, however, are less affected by this, as is evident from the higher average slope of the data in figure 8 than in figure 5. It may be noted that $\overline{\Delta\kappa}$ can also be considered as a measure of the vessel tortuosity, further bolstering the connection between vessel tortuosity and CFL asymmetry.

3.3. *Development of cell-free layer over bifurcations*

On the arterial side of the network, vessels continually bifurcate until the terminal capillaries are reached. The time-averaged CFL profiles are observed to change over

https://doi.org/10.1017/jfm.2019.45 Published online by Cambridge University Press

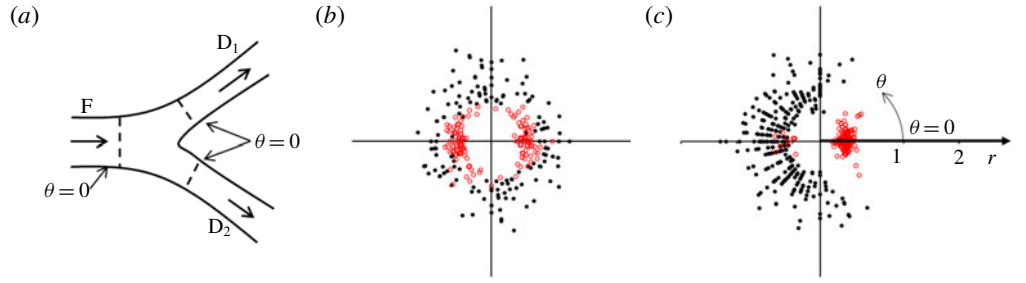


FIGURE 9. (Colour online) (*a*) Schematic of a bifurcation showing the feeding vessel (F), and daughter vessels (D_1 and D_2). Arrows indicate flow directions, and dashed lines indicate upstream and downstream locations where CFL properties are extracted. (*b*,*c*) Polar plots showing how a bifurcation affects the CFL asymmetry. The radial coordinate gives $\overline{\delta}_{max}$ (filled, black circles) and $\overline{\delta}_{min}$ (open, red circles) in μm, while the angular coordinate gives their angular positions ($\theta_{\delta=\delta max}$ and $\theta_{\delta=\delta min}$). As shown in (*a*), for the feeding vessel $\theta = 0$ corresponds to the rightmost side of the vessel; for the daughter vessels, $\theta = 0$ corresponds to the side that is nearest to the bifurcation; $\theta = 0, \pi$ is the plane of bifurcation.

the bifurcations. This is illustrated in figure 9 using polar plots, with the radial coordinate representing $\overline{\delta}_{min}$ or $\overline{\delta}_{max}$, and the angular coordinate representing $\theta_{\delta=\delta\, max}$ or $\theta_{\delta=\delta\, min}$. Data are shown at locations immediately upstream of bifurcations, and at locations immediately downstream of bifurcations (as marked in figure 9*a*). In the discussion and analysis within this section, the $\overline{\delta}_{min}$ and $\overline{\delta}_{max}$ values are computed at $s = L$ in vessels feeding a bifurcation (i.e. locations immediately upstream of the bifurcation), and at $s = 0$ in the daughter vessels (i.e. locations immediately downstream). Owing to the complex geometry, when a vessel bifurcates there is generally a small region at the inlet of a daughter vessel where the diameter is transitioning to its smaller, given diameter. The value $s = 0$ is taken to be the axial location $0.5D$ downstream from the location at the inlet where the vessel first reaches this given diameter. Similarly, $s = L$ in the vessel feeding a bifurcation is defined as the axial location $0.5D$ upstream of the point where the vessel diameter begins to change from that of the feeding vessel.

A clear pattern is noted in the data for the downstream locations: $\overline{\delta}_{min}$ is pre-dominantly localized near $\theta = 0$, which is the side of a daughter vessel closest to the bifurcation, and $\overline{\delta}_{max}$ predominantly occurs in the range $\pi/2 < \theta < 3\pi/2$, that is, near the side farther away from the bifurcation. In contrast, $\overline{\delta}_{min}$ and $\overline{\delta}_{max}$ in the upstream location feeding the bifurcation are not localized, but rather occur all over θ. Thus for most bifurcations, the CFL downstream narrows on the side of the daughter vessel that is closer to the bifurcation, and widens away from this side.

The predominant mechanisms by which the above changes in the CFL over a bifurcation occur are shown in figure 10. The RBC core in the feeding vessel splits as it traverses a bifurcation, and the resulting cores in the downstream daughter vessels are typically shifted towards the inside edge of the bifurcation ($\theta = 0$). This happens because the RBCs from the central region of the feeding vessel directly flow into the daughter vessels via the inside edge of the bifurcation. As a result, the thickness of the CFL is smallest near this edge, but increases towards the opposite side. Additional discussions about figure 10 are provided later.

https://doi.org/10.1017/jfm.2019.45 Published online by Cambridge University Press

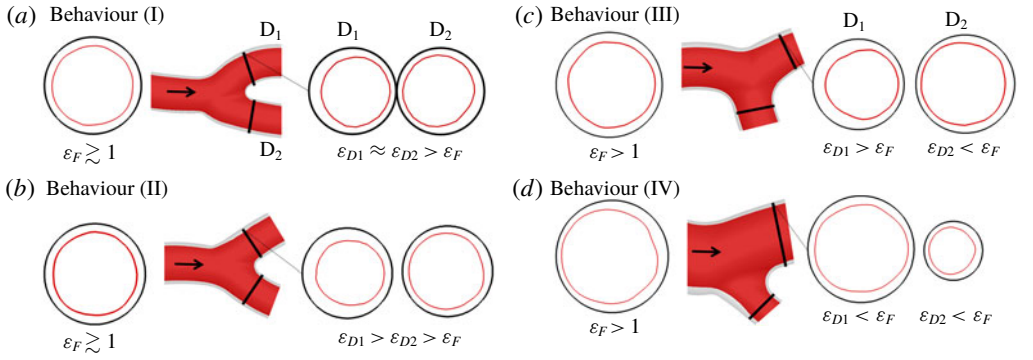


FIGURE 10. (Colour online) Change in the CFL profiles over bifurcations. Cross-sectional profiles are shown upstream (feeding vessel) and downstream (daughter vessels) for four bifurcations. Profiles are looking downstream in the flow direction. (*a*) A nearly symmetric profile in the feeding vessel becomes asymmetric in the daughter vessels as mirror images of one another. (*b*) A nearly symmetric profile upstream becomes more asymmetric in one daughter vessel (D_1) than in the other (D_2). (*c*) An asymmetric profile upstream becomes more asymmetric in one daughter vessel (D_1), but less asymmetric in the other (D_2). (*d*) An asymmetric profile upstream becomes more symmetric in both daughter vessels. In (*a–d*), behaviours labelled I–IV correspond to those identified in the phase diagram of figure 11(*b*).

This change in the CFL characteristics causes a change in the CFL asymmetry between the upstream and downstream locations of a bifurcation. The change in the CFL asymmetry over all bifurcations in the simulated networks is presented in figure 11(*a*) where the asymmetry parameter downstream (ε_{D1} and ε_{D2}) is plotted against the upstream asymmetry ε_F. In figure 11(*a*), the straight line gives $\varepsilon_{D1}, \varepsilon_{D2} = \varepsilon_F$, and the closed and open black circles are data points above and below this line, respectively. Here, 70 % of the data points lie above this line, which shows that in the majority of the bifurcations the asymmetry downstream has increased relative to that upstream. The remaining points which lie below the line, however, show that for these bifurcations the asymmetry decreases in one or both daughter vessels. This will be discussed later.

The change in the CFL asymmetry can be explained by looking at how the RBC core upstream splits into the daughter vessels as it flows through a bifurcation. This is shown in figure 10. As seen in figure 10(*a*), a nearly symmetric CFL profile upstream becomes asymmetric downstream such that the profiles are essentially mirror images of one another. Similar asymmetries in the cross-sectional profiles downstream of a bifurcation have been predicted in theoretical analyses (e.g. Enden & Popel 1994). In figure 10(*b*), the asymmetry increases in both daughter vessels, but this increase is more pronounced in one than the other. Here the CFL profile is nearly symmetric upstream, but the haematocrit profile upstream is skewed towards one daughter vessel. As such, this daughter vessel is on average more filled with RBCs resulting in reduced $\overline{\delta}_{max}$, while the other daughter vessel receives fewer RBCs resulting in an increased $\overline{\delta}_{max}$. In figure 10(*c*), the asymmetry increases in one daughter vessel but decreases in the other. This happens when the CFL profile upstream is already asymmetric. For example, if the upstream profile is shifted to the right, then the asymmetry would decrease in the right daughter vessel since the RBC core is more directly fed into this vessel. For the opposite reason, the asymmetry increases in the left daughter vessel.

https://doi.org/10.1017/jfm.2019.45 Published online by Cambridge University Press

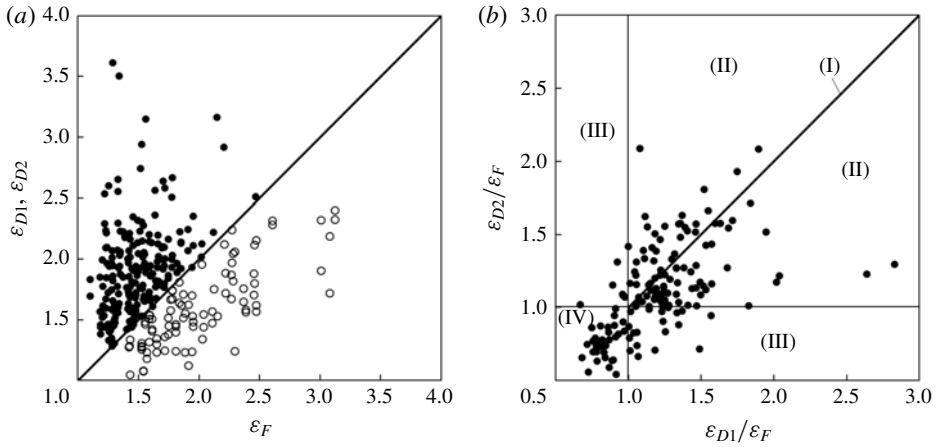


FIGURE 11. (*a*) CFL asymmetry upstream (ε_F) and downstream (ε_{D1} and ε_{D2}) of bifurcations. The straight line gives $\varepsilon_{D1}, \varepsilon_{D2} = \varepsilon_F$, and the closed and open black circles are data points above and below this line, respectively. (*b*) Plot of $\varepsilon_{D1}/\varepsilon_F$ versus $\varepsilon_{D2}/\varepsilon_F$. The regions marked as (I)–(IV) correspond to the behaviours (*a–d*), respectively, as described in figure 10.

Such a discrepancy in the CFL between the daughter vessels is also observed when they have different diameters, with the larger asymmetry typically occurring in the smaller vessel. Lastly, in figure 10(*d*) an asymmetric CFL in the feeding vessel splits into less asymmetric profiles in both daughter vessels. Such behaviour is observed in bifurcations with feeding vessels that are relatively shorter in length, where the effects of the upstream bifurcation come into play, or when one daughter vessel emanates as a small side branch from the feeding vessel. As such, this behaviour is dictated by the geometry. This happens, however, in only a few bifurcations in the network.

The behaviours described in figure 10 are identified in a phase plot in figure 11(*b*), which presents $\varepsilon_{D1}/\varepsilon_F$ versus $\varepsilon_{D2}/\varepsilon_F$. The line marked as (I) represents $\varepsilon_{D1} = \varepsilon_{D2}$ and, hence, the behaviour shown by figure 10(*a*). The regions (II), (III) and (IV) represent the behaviours shown by figures 10(*b*), 10(*c*) and 10(*d*), respectively.

An important conclusion that is readily derived from figure 11(*b*) is that, for many bifurcations, $\varepsilon_{D1} \neq \varepsilon_{D2}$. What this means is that a discrepancy between the CFL asymmetry in the two daughter vessels is commonly observed. This can also be seen in the examples shown in figure 10(*b*,*c*). This discrepancy arises primarily due to the discrepancy in $\overline{\delta}_{max}$ in the daughter vessels. As noted previously in figure 9, the values of $\overline{\delta}_{max}$ at the downstream locations of the bifurcations have a much wider range, while the values of $\overline{\delta}_{min}$ have a very narrow range. It appears, as discussed below, that $\overline{\delta}_{max}$ is dependent on specific haemodynamic conditions which are generally different in the daughter vessels.

We now consider the CFL discrepancy between the two daughter vessels in a bifurcation, and show that it is directly related to cell partitioning at the bifurcation. We consider the difference of $\overline{\delta}_{max}$ between the two daughter vessels, namely $\overline{\delta}_{max,D1} - \overline{\delta}_{max,D2}$, as a measure of the discrepancy of the CFL. Note that this CFL discrepancy between two daughter vessels is not the same as the difference between the CFL thicknesses in two independent isolated vessels, because of the way cells behave near a bifurcation as discussed above. To relate this discrepancy to the cell

https://doi.org/10.1017/jfm.2019.45 Published online by Cambridge University Press

partitioning, one needs to consider not the flow rate or haematocrit, but rather the discrepancy in the flow rates and the RBC fluxes between the two daughter vessels. Note that the flow rate Q and RBC flux N are conserved over a bifurcation, that is, $Q_F = Q_{D1} + Q_{D2}$ and $N_F = N_{D1} + N_{D2}$. The relevant dimensionless quantities are the volume flow ratio (Q^*) and the RBC flow ratio (N^*) between a daughter branch and feeding vessel, defined as

$$Q^*_{D1} = \frac{Q_{D1}}{Q_F} \quad \text{and} \quad N^*_{D1} = \frac{N_{D1}}{N_F} \tag{3.5a,b}$$

for daughter vessel D_1, and similarly for D_2. The computation of these quantities from the simulation data has been described in Balogh & Bagchi (2018). The quantities Q^* and N^* represent how the flow rate and RBCs in the feeding vessel are distributed to the daughter vessels. If $Q^* = N^*$, the RBCs distribute in proportion to the flow rate, and the distribution is called proportionate. Previous studies have shown that, in general, the distribution is disproportionate, that is, $Q^* \neq N^*$. Hence, if $Q^*_{D1} > N^*_{D1}$, then $Q^*_{D2} < N^*_{D2}$, and *vice versa*. This means that, if the flow rate ratio is higher than the RBC flux ratio in one daughter vessel, the opposite is the case in the other daughter vessel. Therefore, when considering the comparative CFL behaviour between the two daughter vessels, in one the flow rate effect will be more pronounced than the haematocrit effect, while in the other it will be reversed. For vessels where Q^* exceeds N^*, the cells will tend to focus more towards the vessel centre, and thus $\overline{\delta}_{max}$ will tend to be greater than in the other daughter vessel where Q^* is less than N^*. Therefore, if $Q^*_1 - N^*_1 > 0$, then $\overline{\delta}_{max,D1} - \overline{\delta}_{max,D2} > 0$, and *vice versa*. This analysis, therefore, suggests that the CFL discrepancy between the daughter vessels in a bifurcation can be directly related to the disproportionality in cell partitioning, i.e. $Q^*_1 - N^*_1$.

In figure 12 we plot $Q^*_1 - N^*_1$ versus $\overline{\delta}_{max,D1} - \overline{\delta}_{max,D2}$. Here we consider those bifurcations that follow the examples shown in figure 10(*a–c*). We do not consider the ones that exhibit the behaviour given by figure 10(*d*). This is because, as noted previously, the CFL behaviour given by figure 10(*d*) is dictated by the geometry, while those given by figure 10(*a–c*) are dictated by flow conditions. As seen in figure 12, for nearly 80 % of the data points, $\overline{\delta}_{max,D1} - \overline{\delta}_{max,D2} > 0$ if $Q^*_1 - N^*_1 > 0$, and *vice versa*, supporting the above analysis that the CFL discrepancy between the daughter vessels can be expressed in terms of the disproportionality in cell partitioning. It may be noted that previous works have shown that CFL thickness in individual isolated vessels is dependent on haematocrit and flow rate (e.g. Kim *et al.* 2007; Fedosov *et al.* 2010). What we have shown here is that it is not the individual Q^* or N^*, but rather $Q^* - N^*$, which represents the disproportionality in cell partitioning, that is directly correlated to CFL discrepancy between daughter branches in a complex network. Additional discussion on phase separation as it pertains to the present results is provided in the next section.

3.3.1. *Influence of the cell-free layer and its symmetry on phase separation*

The quantity $Q^* - N^*$ in the previous discussion quantifies the disproportionality in the flow–cell partitioning behaviour, which is also commonly referred to as phase separation. As mentioned previously, the CFL is related to this phase separation, typically in the context of plasma skimming analyses (e.g. Perkkio & Keskinen 1983; Yan *et al.* 1991; Enden & Popel 1994). In these previous works it is the CFL thickness that is directly related to the plasma skimming phenomenon. Of interest here is the connection between the degree of symmetry of the 3D CFL at

https://doi.org/10.1017/jfm.2019.45 Published online by Cambridge University Press

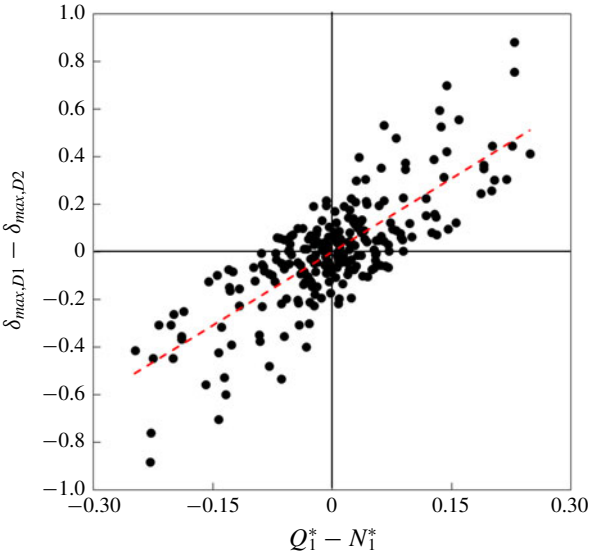


FIGURE 12. (Colour online) A hydrodynamic basis of CFL discrepancy between two daughter vessels downstream of a bifurcation. Plotted here are flow rate and RBC flux discrepancy $Q_1^* - N_1^*$ for one daughter vessel versus the difference in the maximum CFL thickness between the daughter vessels, $\overline{\delta}_{max,D1} - \overline{\delta}_{max,D2}$. The red dashed line is a linear regression of the data.

bifurcations and the degree of phase separation. To investigate this, we plot the CFL asymmetry ahead of a bifurcation (ε_F) versus the degree of phase separation $Q^* - N^*$ in figure 13(*a*). The scatter of the data in this figure suggests that there is no strong correlation between the CFL asymmetry in the feeding vessel and the degree of phase separation. A direct connection between these two quantities would probably exist if the cells were treated as volume-less tracers with a uniform distribution and specified CFL ahead of a bifurcation. This is because, in such a case, any asymmetry in the haematocrit profile is specified by asymmetry in the CFL profile, and it was shown in our previous work (Balogh & Bagchi 2018) that the degree of phase separation at a bifurcation is dictated by the haematocrit profile upstream. Thus, the absence of a strong connection in the current simulations is because ε_F does not necessarily follow the asymmetry of the upstream haematocrit profile. This is due to the finite size of the cells, cell–cell interactions and the influence of bifurcations further upstream.

However, a strong correlation between phase separation and CFL symmetry was observed when we plotted the CFL discrepancy in the daughter vessels ($\overline{\delta}_{max,D1} - \overline{\delta}_{max,D2}$) versus $Q^* - N^*$, as already discussed in the previous section (figure 12).

The quantity that is most directly connected to phase separation is the skewness in the upstream haematocrit profile. This is demonstrated in figure 13(*b*), where we plot the haematocrit skewness in the feeding vessels versus $Q^* - N^*$. The haematocrit skewness S_h at the inlet to a bifurcation is defined as (Balogh & Bagchi 2018)

$$S_h = \text{sign}\left\{\frac{\displaystyle\int_{S_{1/2}} U(r,\theta)\,\mathrm{d}A}{Q_0} - 0.5\right\}\left|\frac{\displaystyle\int_0^r\int_{\theta_1}^{\theta_1+\pi} H_t(r,\theta)\,\mathrm{d}A}{\displaystyle\int_0^r\int_{\theta_1}^{\theta_1+2\pi} H_t(r,\theta)\,\mathrm{d}A} - 0.5\right|. \tag{3.6}$$

https://doi.org/10.1017/jfm.2019.45 Published online by Cambridge University Press

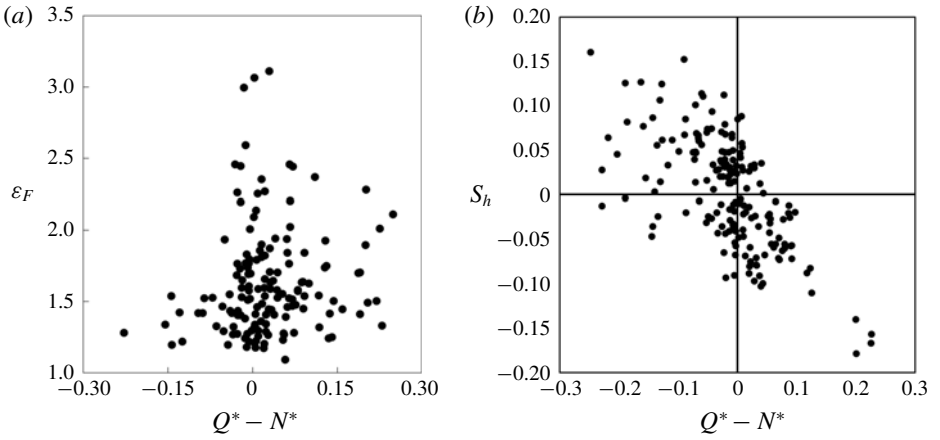


FIGURE 13. (*a*) Degree of phase separation ($Q^* - N^*$) versus asymmetry in the feeding vessel (ε_F) for all bifurcations. The scatter in the data demonstrates the weak connection between these two quantities. (*b*) Haematocrit skewness S_h in the feeding vessel versus degree of phase separation $Q^* - N^*$.

Here, U and H_t are the time-averaged blood velocity and haematocrit over the vessel cross-section at the chosen location, $S_{1/2}$ is the cross-sectional area on one side of the separation surface, and θ_1 to $\theta_1 + \pi$ is the part of the circumference that lies on the same side. The value of S_h represents the fraction of the profile residing on one side of the vessel centreline, while the sign specifies which side. The skewness is positive if the haematocrit profile is skewed towards the daughter vessel that gets more flow, and *vice versa*. Figure 13(*b*) shows that a strong correlation exists between S_h and $Q^* - N^*$. From this figure it can be seen that, as the RBC flow ratio increasingly exceeds the volume flow ratio (i.e. $Q^* - N^* < 0$), a positive haematocrit skewness results, and *vice versa*.

3.4. *Development of cell-free layer over mergers*

On the venous side of a network, starting with the terminal capillaries, vessels continually merge to form larger venules. The CFL profiles are observed to change over the mergers. This is illustrated in figure 14 using polar plots, with the radial coordinate representing $\overline{\delta}_{min}$ or $\overline{\delta}_{max}$, and the angular coordinate representing $\theta_{\delta=\delta\,max}$ or $\theta_{\delta=\delta\,min}$. Data are shown at locations immediately upstream and downstream of the mergers. Note that $\theta = 0, \pi$ is the plane of merger, and that for this section the $\overline{\delta}_{min}$ and $\overline{\delta}_{max}$ values are computed at $s = L$ in vessels feeding a merger (i.e. locations immediately upstream), and at $s = 0$ in the merged vessel (i.e. immediately downstream). At the downstream locations, $\overline{\delta}_{min}$ is predominantly localized near $\theta = 0$ and π, while $\overline{\delta}_{max}$ mostly occurs offset from these regions and around $\theta = \pm\pi/2$. In contrast, upstream $\overline{\delta}_{min}$ and $\overline{\delta}_{max}$ are not localized. This implies that, for most mergers, the CFL downstream narrows in the plane of merger, but widens away from this plane.

The mechanisms by which the change in the CFL occurs over the mergers are identified in figure 15 using two example mergers selected from the simulated networks. For the example in figure 15(*a*), the RBC core downstream is flattened at the top and bottom ($\theta \approx \pi/2, 3\pi/2$). As such, the CFL widens near these locations.

https://doi.org/10.1017/jfm.2019.45 Published online by Cambridge University Press

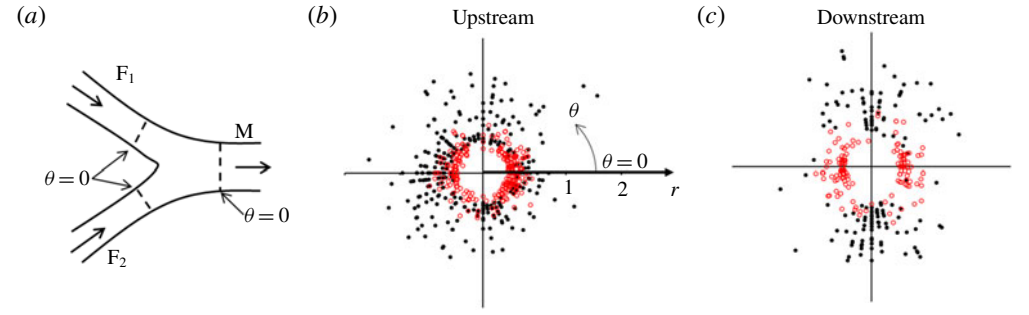


FIGURE 14. (Colour online) (*a*) Schematic of a merger showing the feeding vessels (F_1 and F_2), and the merged vessel (M). For the feeding vessels, $\theta = 0$ corresponds to the side of the vessels nearest to the merger and in the plane of merger. For the merged vessel, $\theta = 0$ corresponds to the right side (looking down the flow direction) of the vessel in the plane of merger. (*b*,*c*) Polar plots showing how CFL changes over the mergers. The radial coordinate gives $\overline{\delta}_{max}$ (filled, black circles) and $\overline{\delta}_{min}$ (open, red circles) in μm, while the angular coordinate gives their angular positions ($\theta_{\delta=\delta\,max}$ and $\theta_{\delta=\delta\,min}$).

This behaviour is reminiscent of the so-called geometric focusing that is observed in vessels with a rapid expansion in diameter (e.g. Faivre *et al.* 2006). An important distinction should be noted when considering geometric focusing in a single vessel as opposed to two merging vessels. For a single vessel with uniformly expanding diameter, the focusing is uniform over the cross-section. However, as our results show, for the mergers the focusing occurs at the top and bottom regions of the merged vessels. This is due to the two merging streams of RBCs which cause the focusing to occur away from the merger plane.

The second mechanism is concerned with the angles at which two feeding vessels merge. As can be seen in figure 15(*a*), in the plane of the merger the CFL downstream is not the same on the right and left sides; it is smaller on the right side than on the left. This happens because the feeding vessel F_2 is nearly perpendicular to the merged vessel, while vessel F_1 is mostly aligned. The CFL on the rightmost side of F_2 decreases as it enters the merged vessel due to the abrupt change in flow direction, or more specifically the abrupt change in curvature on that side of the vessel. The CFL on the leftmost side of F_1 mostly stays the same due to the alignment with the merged vessel (see figure 15*b*). Together, this leads to the unequal narrowing of the profile on either side in the merger plane.

The angle effect can be most easily identified when the flow rates and RBC fluxes from the two feeding vessels are equally balanced, for example, for the merger given in figure 15(*a*,*b*). When the flow rates and RBC fluxes in the feeding vessels are different, their discrepancy contributes to the downstream CFL profile. Another example merger is shown in figure 15(*c*). Here the merged vessel receives approximately 75 % of both the flow and cells from F_1, and 25 % from F_2. Accordingly, the focusing observed is more enhanced on the right side of the merged vessel, which is the side nearest F_2. It is noted that for this example the angle made by each feeding vessel is much smaller than that of the previous example, and thus the narrowing of the profile that occurs in the plane of the merger is nearly equal between the left and right sides. Furthermore, while the contribution fraction from each feeding vessel is different for this example, the distribution is proportionate, or $Q^* \sim N^*$ for both F_1 and F_2. An unequal narrowing between the sides was in

https://doi.org/10.1017/jfm.2019.45 Published online by Cambridge University Press

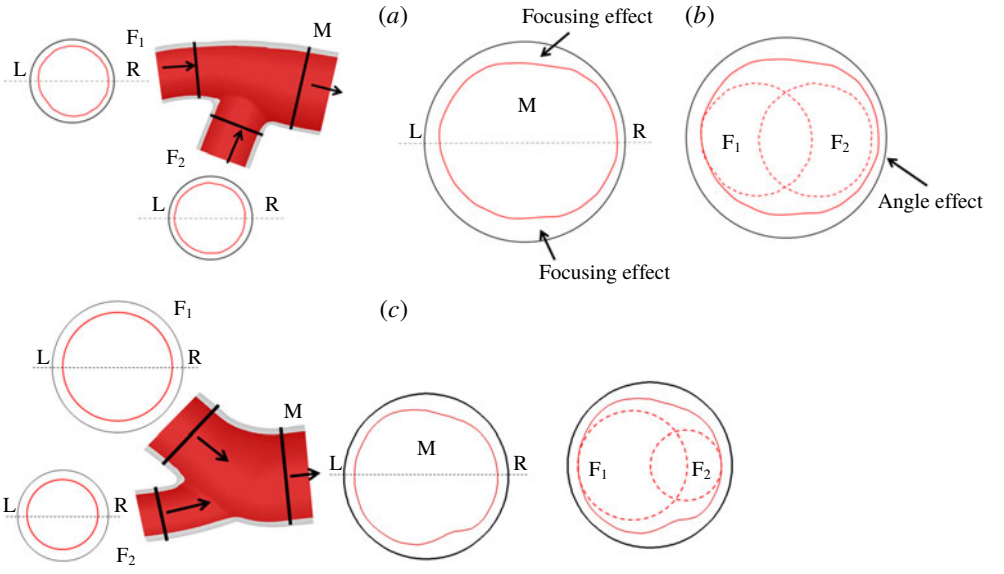


FIGURE 15. (Colour online) Mechanisms of change in CFL profiles over the mergers. Cross-sectional profiles of RBC cores are shown looking downstream in the flow direction. Dashed line is the plane of the merger, and R and L mean right and left sides of a vessel in this plane, respectively. (*a*) Geometric focusing effect results in an increase in the CFL thickness near the top and bottom ($\theta \approx \pi/2, 3\pi/2$) regions of the merged vessel. (*b*) The angle effect. The RBC core in the merged vessel (solid, red line) and those in the feeding vessels (dashed, red lines) are plotted together to show that the CFL changes more on the right side in the plane of merger than on the left side. (*c*) Discrepancy in flow rates and RBC fluxes in the two feeding vessels can cause nearly symmetric upstream CFL profiles to become asymmetric in the merged vessel.

fact observed in mergers with relatively small angles, but this occurred for cases where $Q^* \neq N^*$ for each feeding vessel. This is analogous to what was observed in bifurcations for $Q^* - N^*$ dependence. Here, the CFL thickness was observed to be larger on the side of the merged vessel closer to the feeding vessel with $Q^* - N^* > 0$. Such unequal narrowing was also observed downstream of a merger *in vivo* (Namgung & Kim 2014).

The focusing effect is observed to be more dominant in the simulated networks than the angle effect. It can be isolated by considering the CFL thickness at the top and bottom, $\theta = \pm\pi/2$. Then, the change in the CFL due to focusing alone is quantified by the ratio of the CFL thickness downstream of a merger to that upstream, both evaluated at $\theta = \pm\pi/2$, that is, $\overline{\delta}_{\pm\pi/2,M}/\overline{\delta}_{\pm\pi/2,F1}$ and $\overline{\delta}_{\pm\pi/2,M}/\overline{\delta}_{\pm\pi/2,F2}$. In terms of geometry alone, the focusing effect will depend on the increase in vessel diameter over the merger segment. We introduce a focusing parameter f_p defined as

$$f_p = \frac{r_m - r_f}{l_s}, \tag{3.7}$$

where r_m and r_f are the radii of the merged and feeding vessels, respectively, and l_s is the axial distance between them through the merger. Then, f_p quantifies the rate of increase in vessel size over the merger. In terms of defining l_s, as a vessel merges

https://doi.org/10.1017/jfm.2019.45 Published online by Cambridge University Press

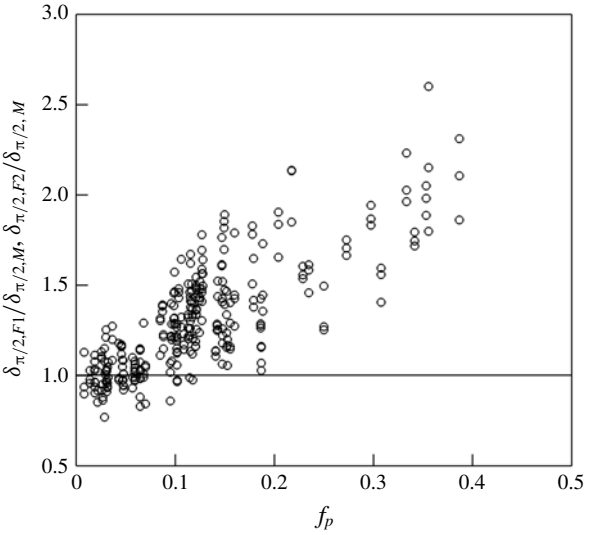


FIGURE 16. The focusing effect on the change in the CFL over the mergers. Plotted here is the focusing parameter f_p versus $\overline{\delta}_{\pm\pi/2,M}/\overline{\delta}_{\pm\pi/2,F1}$ and $\overline{\delta}_{\pm\pi/2,M}/\overline{\delta}_{\pm\pi/2,F2}$.

and expands in diameter, the inlet of the merger is defined as that $0.5D$ upstream of the axial location at which the vessel diameter began to increase. Similarly, the outlet is defined as $0.5D$ downstream from the axial location at which the merged vessel diameter has increased to its given value. The focusing effect is expected to increase with increasing rate of diameter change, and would be the maximum for an abrupt change in diameter. In figure 16, we plot f_p versus $\overline{\delta}_{\pm\pi/2,M}/\overline{\delta}_{\pm\pi/2,F1}$ and $\overline{\delta}_{\pm\pi/2,M}/\overline{\delta}_{\pm\pi/2,F2}$ for all mergers. As is evident, for most mergers the ratio is greater than one, and it increases with increasing f_p.

Finally, we quantify the change in CFL over the mergers by considering the CFL asymmetry upstream in the feeding vessels, ε_{F1} and ε_{F2}, and downstream in the merged vessel, ε_M. Figure 17 shows ε_{F1} and ε_{F2} versus ε_M. For more than 70 % of the feeding vessels, the asymmetry increases over the mergers. The increase in asymmetry is primarily caused by the focusing and angle effects as noted before, in conjunction with cell–flow discrepancies. For some mergers, the asymmetry decreases in the merged vessel relative to the feeding vessel. This occurs in feeding vessels with proportionate cell–flow distributions that have small values of f_p so that the focusing effect is small, or vessels that are aligned with the merged vessel so that the angle effect is small. Furthermore, if the asymmetry in the feeding vessel is such that $\overline{\delta}_{max}$ occurs near $= 0$, and $\overline{\delta}_{min}$ occurs near $\theta = \pi$, then the CFL profile in the merged vessel is generally more symmetric.

3.5. *Connection between cell-free layer and flow resistance*

It is generally accepted that a smaller CFL thickness tends to correspond to an increased flow resistance, and *vice versa*. This follows from the idea that an increase in haematocrit, which generally correlates to a decreased CFL thickness, results in an increased viscosity (e.g. Fedosov *et al.* 2010).

For the present work, a strong correlation was observed in the relationship between time-averaged CFL thickness per vessel (i.e. $\overline{\overline{\delta}}$) and the time-averaged vessel flow

https://doi.org/10.1017/jfm.2019.45 Published online by Cambridge University Press

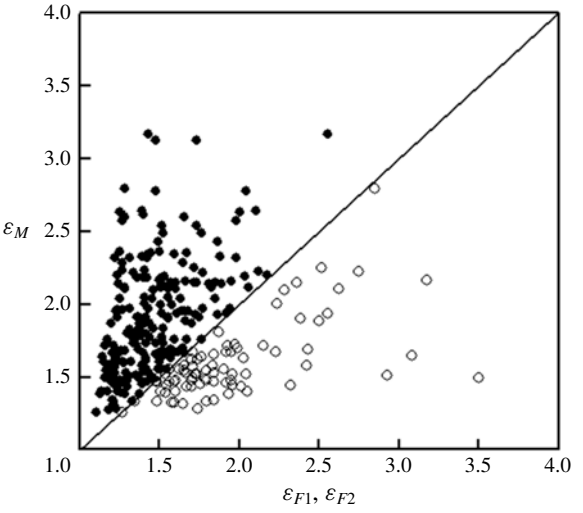


FIGURE 17. Change in CFL asymmetry over the mergers. CFL asymmetry upstream of the mergers (in the feeding vessels) ε_{F1} and ε_{F2} versus that downstream (in the merged vessel) ε_M is plotted. The straight line represents $\varepsilon_{F1}, \varepsilon_{F2} = \varepsilon_M$. Filled and open circles represent increase and decrease, respectively, in CFL asymmetry.

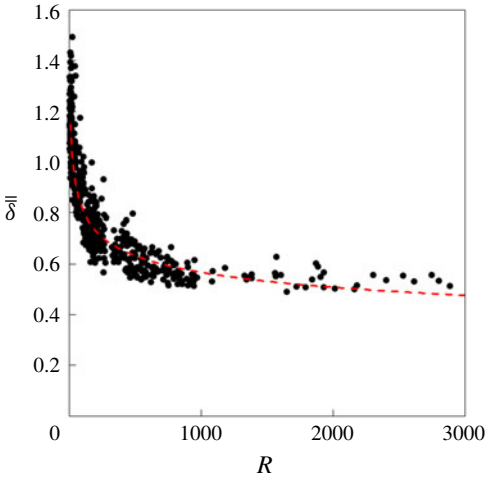


FIGURE 18. (Colour online) Time-averaged CFL thickness ($\bar{\bar{\delta}}$) versus resistance per length (R). Each data point is for an individual vessel, with data given for all simulations. The $\bar{\bar{\delta}}$ value is given in μm, while R is given in Pa $(\mathrm{m}^3\ \mathrm{s}^{-1})^{-1}\ \mu\mathrm{m}^{-1} \times 10^{-11}$. The dashed red line is a power regression given by $\bar{\bar{\delta}} = 1.692R^{-0.158}$, with a correlation coefficient of 93 %.

resistance, R. Figure 18 provides a plot of $\bar{\bar{\delta}}$ versus R for all vessels in the networks. As in Balogh & Bagchi (2017*b*), R is calculated as $R = \Delta P'/Q$, where $\Delta P'$ is the vessel pressure drop per length, and Q is the volume flow rate.

This generally shows the expected trend that CFL thickness decreases with increasing flow resistance. It is also evident from figure 18 that the relationship

https://doi.org/10.1017/jfm.2019.45 Published online by Cambridge University Press

between $\overline{\overline{\delta}}$ and R follows a power law. This type of behaviour is expected, as it is generally in line with the well-known power-law relationship between CFL thickness and viscosity as given by the core–annular blood flow model (Pozrikidis 2003). However, we did not notice any correlation between CFL asymmetry and flow resistance. This may be due to the highly complex nature of the spatial variation in the CFL as discussed previously.

3.6. *Red blood cell migration trends, and effects of geometry*

It is widely accepted that the CFL arises in vessels as the net result of the balance between a number of forces (Coupier *et al.* 2008; Kumar & Graham 2012; Zhao *et al.* 2012; Grandchamp *et al.* 2013; Katanov *et al.* 2015; Secomb 2017). Most prominent among these is a lift force on the cells away from the walls due to their deformability and wall effects, which is countered by a shear-induced diffusion arising from the interactions between cells which tends to disperse them over the cross-section. In terms of quantifying this balance and elucidating the underlying physics, a straight tube or channel provides an ideal framework, as considered in the aforementioned studies. For example, Katanov *et al.* (2015) in their simulations of RBCs in a straight tube, utilized a theoretical model to quantify this in terms of a balance between pressures on the RBC core; an outward pressure force within the RBC core due to cell collisions was balanced by a compressive pressure force on the surface of the RBC core due to the lift and other repulsive forces. Grandchamp *et al.* (2013) studied the lift and shear-induced diffusion components in separate experimental studies specifically designed to capture these. The lift component was studied in a Couette shear flow device, and they found that tumbling RBCs follow the same scaling laws as tank-treading RBCs with regard to the migration velocity. For diffusion, this involved an RBC suspension flowing through a microfluidic channel, and different diffusivities were found in the shear and vorticity directions.

However, unlike in a straight tube or channel, in a network of interconnected and winding vessels it is difficult to isolate the lift and diffusion components, for several reasons. First, the idea behind diffusion is generally based on the interactions between multiple cells (often, multiple layers of cells spanning the vessel cross-section) over long vessels. Approximately 76 % of the vessels in the simulated networks are less than 12 μm in diameter; thus the RBC lateral diffusion will be highly hindered. Furthermore, in approximately 70 % of vessels RBCs are observed to flow in either a single- or double-file manner. So the actual meaning of shear-induced diffusion in these vessels is questionable.

Second, diffusion is generally a slow process. For example, Katanov *et al.* (2015) studied CFL development along the length of a tube, and mentioned an initial fast time scale corresponding to RBC migration away from the wall, and a second slower time scale related to cell–cell interactions. The authors showed that the axial length required for the full development was approximately 25 times the tube diameter. Based on Zhao *et al.* (2012), it requires approximately 70 equivalent diameters for the haematocrit profile to become stationary. In contrast, the ratio of length to diameter for the vessels in our simulated networks is typically in the range of 5–10, which is significantly less than the axial lengths required for the diffusion to fully establish. One consequence of these factors is that the predicted CFL in many vessels in the networks does not relax to a symmetric profile, as seen in figures 3 and 4.

Third, the shear-induced diffusion and other factors affecting the CFL are functions of haematocrit and shear rates. Accordingly, the aforementioned balance of lift and

https://doi.org/10.1017/jfm.2019.45 Published online by Cambridge University Press

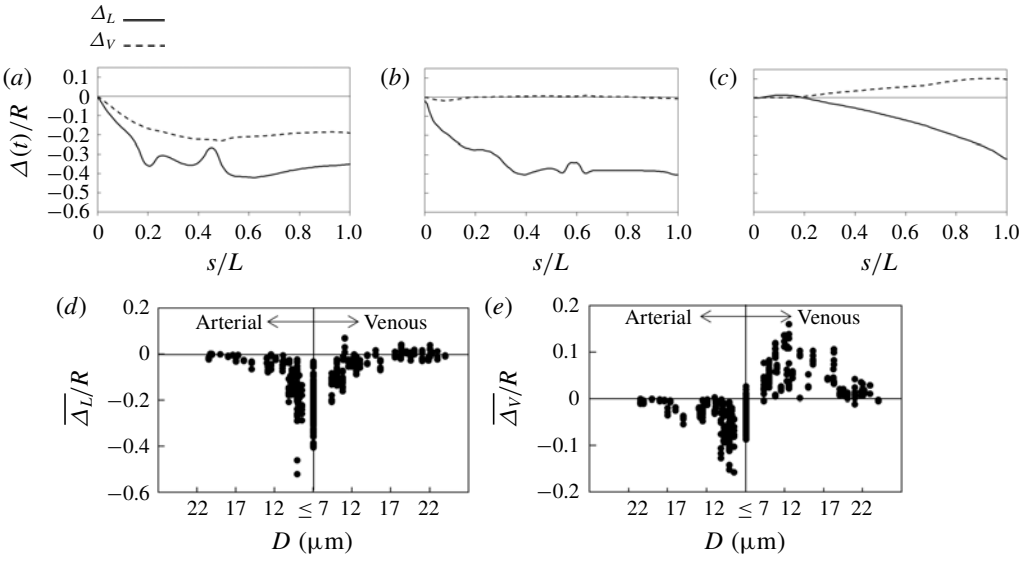


FIGURE 19. In-plane ($\Delta_L(t)/R$) and out-of-plane ($\Delta_V(t)/R$) radial displacements of RBCs. (*a–c*) Time-dependent displacements of an RBC in an arteriole, capillary and venule, respectively, as a function of RBC axial location scaled by vessel length, s/L. (*d*,*e*) Average displacements of RBCs in each vessel.

diffusion is generally studied for a given vessel haematocrit and shear rate (e.g. Katanov *et al.* 2015; Kruger 2016). In our simulated networks, we do not control haematocrit and shear rates in individual vessels. These two quantities vary in space and time, even within a single vessel. This makes it difficult to define a representative shear rate or haematocrit per vessel in a consistent manner.

Because of these complexities, the microvascular networks simulated here are not the appropriate framework to study the balance of lift and shear-induced diffusion. In order to isolate these two factors and systematically study the effect of geometry, one needs to consider an idealized and well-defined geometry, such as a curved tube with a constant curvature. This is beyond the scope of the current study as the networks considered here are naturally very irregular.

However, the result of the balance between hydrodynamic lift and shear-induced diffusion is closely related to the radial displacement of the cells, which can be quantified from our simulations. Radial displacement of each individual cell as it traverses a vessel, as well as the average displacement of all cells traversing a vessel, are directly related to the CFL. Given the planar nature of the networks, we consider two components of radial displacement: the in-plane component $\Delta_L(t)$ representing the displacement of a cell centroid in the plane intersecting the vessel centrelines, and the out-of-plane component $\Delta_V(t)$ that is normal to this plane. Both are computed relative to the initial radial position when a cell entered the vessel. The time signals for $\Delta_L(t)$ and $\Delta_V(t)$ as computed for an individual RBC flowing through three representative vessels are shown in figure 19(*a–c*), for an arteriole, a capillary and a venule, respectively. A positive displacement means cell motion towards the vessel wall, and *vice versa*. For each of these vessels, the in-plane components are negative, meaning the cell moves away from the wall. The displacements for the vessels in figure 19(*a*,*b*) are not monotonic, and, following § 3.2, the variations arise due to the

https://doi.org/10.1017/jfm.2019.45 Published online by Cambridge University Press

vessel curvature. In contrast, the out-of-plane component is negative in the arteriole, nearly negligible in the capillary, but positive in the venule. Overall, the general picture that arises is that, for the in-plane displacement, the direction is away from the walls, with fluctuations occurring due to vessel curvature. For the out-of-plane component, it tends to be away from the wall in vessels on the arterial side, but opposite on the venous side.

Figure 19(*d*,*e*) presents displacements averaged over all cells for each vessel, versus vessel diameter. As can be seen, the in-plane component tends to be negative in all vessels, while the out-of-plane component tends to be negative in arteries and positive in venules.

The explanation for the observed in-plane migration trends follows from what has been presented in §§ 3.3 and 3.4 in terms of cell behaviour at bifurcations and mergers. Regarding trends within arteries and capillaries, as RBCs enter a daughter vessel of a bifurcation, they flow near the side of the vessel that is closer to the bifurcation. This resulted in the minimum CFL thickness occurring on the side of the cross-section nearest the bifurcation. At this location, the cells experience a large velocity gradient, and a large hydrodynamic lift, resulting in a fast radial movement away from the wall. This can be seen in figure 19(*a*,*b*), and is in agreement with the observation of Katanov *et al.* (2015). Regarding trends within venules, at the exit of mergers RBCs tend to flow closer to the side nearest the feeding vessel from which they came. This initial near-wall position in the venule is also conducive to a greater in-plane displacement from the wall. For all vessels, over the lengths the vessel curvature modulates the in-plane displacement of the cell.

The trends observed for the out-of-plane component are also due to the geometry of the networks. As cells in vessels on the arterial side flow through a bifurcation and into a smaller-diameter vessel, the initial position tends to be near the upper and lower portions of the cross-section. This happens because of the relative increase in confinement due to the decrease in diameter. As the cells proceed along the length they subsequently migrate inwards, away from the wall. In venules, the average outward migration of the cells can be explained by a similar but opposite feature of the geometry. That is, as the cells flow through a merger and into a larger-diameter vessel, the initial position of the cells is relatively closer to the centreline. The CFL profile associated with the geometric focusing effect identified in § 3.4 is suggestive of a lower concentration near the upper and lower portions of the cross-section. This then lends itself to generally promoting out-of-plane motion towards the walls in venules.

We further investigate the relation between the total lateral (cross-stream) distance travelled by the cells in a vessel and the cumulative change in the CFL asymmetry (figure 20). As can be seen, a positive correlation is observed. It was shown in figures 5 and 8 that CFL asymmetry increases with increasing vessel tortuosity. Therefore, figure 20 implies that as vessel tortuosity increases, so does the average cross-stream movement of RBCs, and the asymmetry in the CFL.

Overall, these trends observed in the RBC migration tendencies further demonstrate that the most significant factors dictating the observed CFL patterns in the networks are the specific geometric features of the vasculature, such as bifurcations, mergers and vessel tortuosity.

4. Additional discussion

4.1. *Generality of results*

The design of each of the microvascular networks, while based on *in vivo* images and data, does not represent any specific network from a particular organ of a particular

https://doi.org/10.1017/jfm.2019.45 Published online by Cambridge University Press

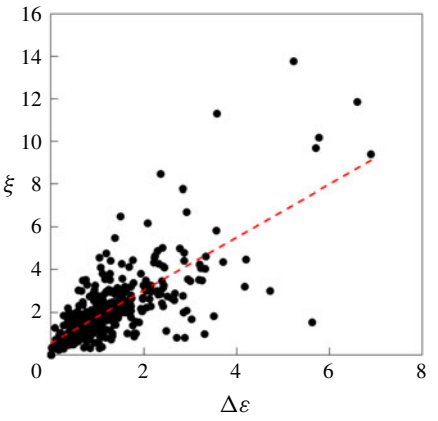


FIGURE 20. (Colour online) Average lateral distance ξ (in μm) travelled by all cells in each vessel versus cumulative change in CFL asymmetry $\Delta\varepsilon$ as presented in figure 3. The dashed line is a linear regression.

animal. Their features are in line with *in vivo* microvasculature architectures in the sense that they include winding, interconnected vessels with lengths and diameters in general agreement with and of the same order as what occurs *in vivo*. Details can be found in Balogh & Bagchi (2017*b*). The three networks as considered here were developed to be inclusive in terms of the diverse features of microvascular networks *in vivo*. A comparison of different haemodynamic quantities predicted from the model and obtained *in vivo* in specific organs of different animals shows a good agreement (Balogh & Bagchi 2017*b*), suggesting the generality of the simulated networks. Such generality can be further demonstrated using the predicted CFL thickness. A comparison between average CFL thickness values per vessel and that reported *in vivo* from different studies is presented in appendix A. As noted therein, the *in vivo* thicknesses come from different organs and/or different animals, and as such do not come from one particular kind of network geometry. Yet, a general agreement between the simulation results and *in vivo* values is observed, which provides a quantitative measure that demonstrates generality in this sense, in terms of the CFL thickness. The generality of the results can also be shown in terms of other hydrodynamic quantities. A comparison between the hydrodynamic resistance in each vessel from the simulations with reported *in vivo* data from the mesentery of a cat (Lipowsky *et al.* 1978) is provided in the supplementary material. Also included is a comparison between the time-averaged wall shear stress in each vessel from the simulations with *in vivo* data from networks in the human retina (Koutsiaris *et al.* 2007). While from different animals and organs, each of these agreed well with the *in vivo* data, providing a further quantitative measure of the generality.

Generality can also be demonstrated in a phenomenological sense, by considering phase separation at bifurcations. In Balogh & Bagchi (2018), cell partitioning at bifurcations was studied in the present networks, and disproportionate partitioning was predicted to a widely varying degree. Such disproportionality is a hallmark of microvascular blood flow, as has been observed *in vivo* in a wide variety of network topologies not specific to any particular organ or animal.

https://doi.org/10.1017/jfm.2019.45 Published online by Cambridge University Press

4.2. *Influence of entrance haematocrit*

As discussed in § 2, for each of the simulations the haematocrit is maintained in the main feeding artery at approximately 30 %. We did not perform a parametric study by varying the feeding artery haematocrit, because the chosen value corresponds to a typical tube haematocrit under normal physiological conditions. The objective of the current study is to represent a physiological situation as best as possible. Thus, a parametric study by varying the feeding artery haematocrit is not considered. Choice of a different inlet haematocrit value would possibly affect the CFL thickness, but not necessarily the CFL behaviours (such as the 3D structure) as discussed here. It may also be noted that, although the feeding artery haematocrit is maintained at 30 %, haematocrits in different vessels in the networks show large differences (e.g. see Balogh & Bagchi 2017*b*), as is the case *in vivo*. These haematocrit values in individual vessels in our simulated networks arise naturally because of the way cells are partitioned at each bifurcation; they are not specified or varied. Nevertheless, the effect of this inlet haematocrit value on the results could be of interest; however, given the extensive computation required for the present simulations, this is left for future work.

4.3. *Influence of vessel diameter*

The vessel diameters in the networks vary over a significant range as noted in § 2. It was generally observed that the average CFL thickness increased with increasing diameter (table 1 of appendix A), which is an expected trend. Aside from this, analysis of the three-dimensionality of the CFL, as well as the behaviour along vessel length and through bifurcations and mergers, did not exhibit prominent trends when considering the influence of diameter itself, as discussed below.

Along vessel lengths, trends in the asymmetry variation most strongly depended on the vessel curvature. Granted, the vessel curvature used for the analysis in § 3.2 was non-dimensionalized by the vessel radius, which introduces some dependence on diameter, this was done merely to provide a consistent scale for comparing results between all vessels. At bifurcations, the only notable diameter dependence was with regard to behaviour (III) in figure 10(*c*). As noted in § 3.2, for bifurcations with daughter vessels of different diameter, an asymmetric inlet profile was observed to result in an increased asymmetry in the daughter vessel with the smaller diameter. This was because the inlet asymmetry was typically such that the RBC core was shifted towards the larger daughter vessel as it generally received a greater fraction of the flow. Because the RBC core was then more directly fed into the larger-diameter vessel, the smaller daughter vessel had an increase in CFL asymmetry. For mergers, the influence of diameter comes into play with the focusing parameter, where as per (3.7) the difference in radius between the feeding and merged vessels was directly proportional to f_p. In this sense, for a given distance through a merger, a greater increase in diameter would lead to a greater focusing effect.

4.4. *Potential impact of red blood cell aggregation*

The present model does not account for RBC aggregation. As such, the simulations represent a period of time during which RBC aggregates do not form in the simulated section of the microvasculature. While aggregation is known to occur at low shear rates or under diseased conditions, it has also been shown to occur under normal physiological conditions involving high shear rates (Brust *et al.* 2014). Consideration

https://doi.org/10.1017/jfm.2019.45 Published online by Cambridge University Press

of RBC aggregation, and its potential role in stabilizing clusters of cells, may influence the CFL behaviours observed in the present work, as discussed below.

In general, RBC aggregation has been shown to increase the thickness of the CFL (e.g. Reinke *et al.* 1987; Ng *et al.* 2016). This is because the resulting RBC clusters tend to flow more within the central core region of vessels. With regard to the CFL development over bifurcations, this could affect the entrance profiles observed in figure 10, and, in turn, the daughter branch profiles. Ong *et al.* (2010) showed that RBC aggregation caused CFL thicknesses on either side of a daughter branch to be affected differently, which provides evidence that the degree of 3D asymmetry observed here may change. Though the general behaviours described in figure 10 would still exist, it is possible that the magnitudes of the asymmetries may vary. Another consideration is that, in the smallest capillary bifurcations, where the cells must significantly deform to enter, as clusters of cells caused by RBC aggregation pass through, this may lead to a reduced asymmetry in daughter vessels. Without aggregation, RBC clusters may break up as they squeeze to enter the smallest bifurcations, causing the cells to flow in one-by-one shifted to the side of the daughter vessel. Aggregation-stabilized RBC clusters may more easily flow as a group and thus more uniformly fill the cross-section.

RBC aggregation could also lead to an increased variation in asymmetry along the length of a vessel due to curvature-induced migration. Aggregation-derived attraction forces are known to enhance axial migration effects (Kim, Ong & Johnson 2009*a*), which could increase the degree to which the RBC core shifts following the vessel curvature. RBC aggregation may also potentially enhance the geometric focusing effect observed at the outlet to mergers. If the cells in the vessels feeding the merger are on average located more within the central core region, then as the vessels merge the CFL thickness associated with the focusing effect may become more pronounced.

5. Conclusions

A detailed quantitative analysis is presented on the near-wall RBC-free layer based on high-fidelity simulations of cellular-scale blood flow in microvascular networks with *in vivo*-like topologies. The simulated networks comprise multiple bifurcations, mergers and winding vessels. Unlike previous studies, which primarily focused on the CFL development in single, isolated vessels, or isolated bifurcations or mergers, the present work allows us to study the CFL as it develops naturally in a complex network. Furthermore, unlike in fully developed flows in straight tubes where the CFL is axisymmetric, the geometric complexity and the heterogeneity in haemodynamic quantities in the vascular networks make the CFL highly 3D and non-axisymmetric. In this article we fully quantify the 3D asymmetric nature of the CFL and identify the mechanisms that lead to such complexities in different facets of the networks, namely, along the vessel lengths, and over the bifurcations and mergers. The new findings from this study are summarized below.

We have shown that the CFL is distinctly 3D and asymmetric, and significantly varies over all aspects of the networks. Such complexity occurs in both space and time, while the primary focus here has been on the time-averaged CFL. Its highly asymmetric nature has been quantified by means of an asymmetry parameter that was observed to vary along the vessel length significantly. Such variations were predominantly non-monotonic, which indicated that CFL profiles did not simply become more symmetric over the length, but rather continuously fluctuated in its degree of asymmetry. Furthermore, the shape of the CFL profile associated with

https://doi.org/10.1017/jfm.2019.45 Published online by Cambridge University Press

the changing asymmetry was quantified by the angular locations of the maximum and minimum thicknesses. These angular locations were also shown to significantly fluctuate over the length, thus providing further quantitative insight into the highly 3D and asymmetric nature of the CFL in the networks.

We have shown that vessel tortuosity causes the CFL to vary significantly along the length. We have specifically identified a curvature-induced migration of the RBCs, which causes the CFL to be smaller on the side of the vessel with smaller local arclength. Furthermore, we have shown that the changes in vessel curvature can locally enhance the CFL.

The vascular bifurcations are observed to change the CFL profile, and in the majority of them the CFL asymmetry increases. This is generally observed to occur such that the CFL downstream narrows on the side of the vessel nearest the upstream bifurcation, and widens on the other side. While such behaviour has been observed previously, the present study elucidates the 3D nature. Specifically, four different behaviours are identified which characterize the means by which the CFL changes over the bifurcations. For many bifurcations, a discrepancy exists between the CFL asymmetry in the daughter vessels. A hydrodynamic basis underlying the discrepancy is presented that arises from a disproportionate partitioning of the flow rate and RBC flux in the daughter vessels.

Similar to the bifurcations, the mergers also change the CFL profile, and in the majority of them the asymmetry increases. For most mergers the downstream CFL narrows in the plane of the merger, but widens away from this plane. The mechanisms by which such changes occur are identified as a geometric focusing of two merging streams, and an angle effect associated with the relative orientation of each merging stream. The former causes an enhanced CFL out of the plane of the merger, while the latter causes an unequal narrowing of the CFL on either side in the merger plane. While collectively these contribute to the changing CFL, the focusing effect is observed to be dominant.

These findings have important haemorheological and other biophysical implications. The highly varying and asymmetric CFL profiles suggest a highly varying and asymmetric viscosity field near the vessel walls, which would eventually affect the apparent viscosity of blood, both at the level of individual vessels as well as at the whole network level. This and, in particular, the finding of the curvature-induced migration could motivate theoretical works for low-dimensional models of blood viscosity in curved vessels. In terms of biophysical implications, the results suggest that the margination of platelets, leukocytes and other elements such as drug particulates may be impacted, especially in regions of enhanced CFL due to curvature-induced migration. Because these cells and particles are more rigid than RBCs, they would be less affected by this geometry-induced migration and could marginate faster in the regions of locally enhanced CFL. The highly varying and asymmetric nature of the CFL also suggests that such local variations in wall shear stress may occur. This would probably cause a heterogeneity in the endothelial cell response over individual vessels. The present findings also suggest that certain regions in microvascular networks may be more susceptible to NO scavenging than others, as the CFL provides a barrier inhibiting this. For example, the consistent narrowing of the CFL observed on one side of vessels downstream of the bifurcations may represent a local region of increased NO scavenging, as would the sides of vessels with a relatively small radius of curvature. The present work could motivate investigation of these subtle but important issues.

https://doi.org/10.1017/jfm.2019.45 Published online by Cambridge University Press

Acknowledgements

This study is supported by a grant (CBET 1604308) from the National Science Foundation. Computational support is provided by the NSF's XSEDE resources at Texas Advanced Computing Center.

Supplementary material

Supplementary material is available at https://doi.org/10.1017/jfm.2019.45.

Appendix A. Cell-free layer calculation procedure

The procedure developed for calculation of the CFL in the present work is illustrated in figure 21. For each simulation, data are stored at 0.5 ms intervals, with approximately 1400 instants in total. Each dataset stored gives a 3D snapshot of the shape of all RBCs in the entire network. A number of such consecutive snapshots are first superimposed to generate an instantaneous RBC core. The RBC core is the resulting shape traced out by all the RBCs moving through a vascular segment of interest over a small window of time approximately corresponding to the RBC transit time through that segment. This time window also corresponds to the smallest time so that no plasma gap appears between the cells along the axial direction. The influence of this time window was verified by increasing its range and considering the time-dependent CFL patterns and thicknesses. The differences were insignificant. The effect on time-averaged CFL characteristics was also insignificant. Once the instantaneous core is traced out, the space between the core and the vessel wall gives the instantaneous CFL. Physically, it represents the space that is completely devoid of cells over the aforementioned time window. The thickness of the CFL, denoted by δ, is the distance between the core and the vessel wall, and is measured at each vertex of the surface mesh used to discretize the vascular walls. The resulting instantaneous CFL thickness $\delta(s, \theta, t)$ is 3D, and is a function of axial position s along a vessel length, angular position θ on the vessel cross-section, and time t, as shown in figure 21(*c*,*d*). The axial coordinate s increases from vessel inlet ($s = 0$) to outlet ($s = L$), and the angular position θ is defined looking downstream along the flow direction. The time-averaged CFL thickness is determined by averaging $\delta(s, \theta, t)$ over the entire simulation time, and is denoted by $\overline{\delta}(s, \theta)$; thus, the 3D nature of the CFL is retained in the time-averaged value.

To validate the present approach for determining the CFL, comparisons are made with previous experimental measurements of CFL thickness as a function of vessel diameter. The average CFL thickness is determined for each vessel as

$$\overline{\overline{\delta}} = \frac{1}{2\pi L} \int_0^L \int_0^{2\pi} \overline{\delta}(s, \theta)\, \mathrm{d}\theta\, \mathrm{d}s, \tag{A 1}$$

where L gives the length of the vessel. We compare the CFL thickness for different ranges of vessel diameter as presented in table 1. The smallest vessels in our networks are 6 μm in diameter, and among these the CFL thickness was calculated to range from 0.5 to 0.8 μm. This is in good agreement with that reported in the *in vivo* work of Tateishi *et al.* (1994), where the CFL thicknesses in 6 μm vessels were reported to range from approximately 0.5 to 0.9 μm. For larger vessels in our networks less than 10 μm in diameter, the CFL thickness was calculated to range from 0.6 to 1.0 μm. This is in good agreement with the *in vivo* work of Soutani *et al.* (1995),

https://doi.org/10.1017/jfm.2019.45 Published online by Cambridge University Press

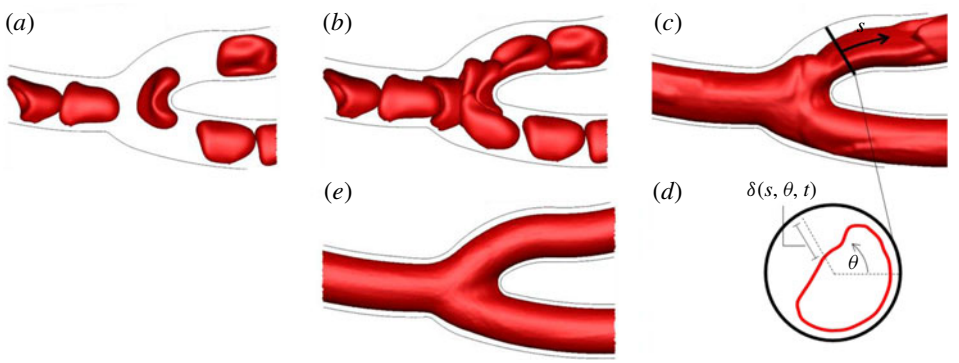


FIGURE 21. (Colour online) Computation of 3D CFL. (*a*) An image of RBCs at one time instant in a bifurcation of a simulated network. (*b*) Superposition of RBCs at a few consecutive time instants. (*c*) Instantaneous RBC core as obtained by superimposing the RBCs over a small time window. (*d*) Cross-sectional view of the instantaneous RBC core and CFL. (*e*) Time-averaged RBC core.

where thicknesses ranging from approximately 0.7 to 1.1 μm were reported for vessels in this diameter range. For vessels in the simulations between 10 and 24 μm in diameter, $\overline{\overline{\delta}}$ was calculated to range from 0.8 to 1.5 μm. In this diameter range, the *in vivo* work of both Soutani *et al.* (1995) and Kim *et al.* (2007) reported values ranging from approximately 0.8 to 2.0 μm. This also generally agrees with that determined in Pries *et al.* (1989) based on a theoretical estimation utilizing *in vivo* data. Comparisons against additional experimental measurements are also given in table 1, which shows that the CFL thickness predicted with the present methodology is in good agreement with that observed *in vivo*. It is noted that haematocrit in the largest feeding arterioles for the present simulations was approximately 30 %. The CFL thickness values reported from other works are based on the same haematocrit, with the exception of the data of Bloch (1962) and Copley & Staple (1962) where the haematocrit values were not reported, and Kim *et al.* (2007) where the haematocrit was approximately 40 %. Regarding flow rates, *in vivo* works have typically reported these in terms of RBC velocities. In the simulations the velocities range from 0.2 to 2.7 mm s^{-1} over all vessels. This is similar to those observed in the study of Tateishi *et al.* (1994), where values ranged from 0.2 to 2 mm s^{-1} reported over a range of diameters from 6 to 40 μm. Bloch (1962) reported velocities ranging from 1.98 to 2.41 mm s^{-1} for 9 μm diameter vessels, 0.74 to 2.16 mm s^{-1} for 13 μm vessels, and 1.67 to 4.5 mm s^{-1} for 16 μm vessels, which are also similar to that observed in the simulations. Kim *et al.* (2007) reported relatively higher velocities ranging from 6.1 to 11.1 mm s^{-1}. However, these are values averaged are over all vessels in their study, which ranged in diameter from approximately 10 to 60 μm.

For the haematocrits and flow rates in the noted *in vivo* works, we are not able to directly match these based on individual vessel diameters as they were not reported in a manner conducive to this. As discussed, for haematocrit, some works did not report values, while others reported only one value for the entire study over the range of vessel diameters considered. For flow rates the situation was similar. While Bloch (1962) did report some velocities in terms of a specific diameter, it was only reported for three of the diameters considered, and they did not report any haematocrit values. In spite of these issues, what we consider here is that, because our haematocrits and

https://doi.org/10.1017/jfm.2019.45 Published online by Cambridge University Press

Vessel diameter (μm)	$\overline{\overline{\delta}}$ (μm) Present	*In vivo*	Authors	Organ	Animal
5–6	0.5–0.8	0.8–1.2	Bloch (1962)	Mesentery	Rat
		0.5–0.9	Tateishi *et al.* (1994)	Mesentery	Rabbit
7–10	0.6–1.0	0.9–1.5	Bloch (1962)	Mesentery	Rat
		0.7–1.1	Soutani *et al.* (1995)	Mesentery	Rabbit
11–24	0.8–1.5	1.3–4.5	Bloch (1962)	Mesentery	Rat
		0.6–3.5	Copley & Staple (1962)	Cheek pouch	Hamster
		0.9–1.8	Soutani *et al.* (1995)	Mesentery	Rabbit
		0.8–2.0	Kim *et al.* (2007)	Muscle	Rat

TABLE 1. Comparison between time-averaged CFL thickness $\overline{\overline{\delta}}$ computed from simulations and that determined *in vivo* by various authors.

flow rates are generally in a similar physiological range as the *in vivo* studies, this provides a basis for a point of comparison with regard to average CFL thicknesses. Complete details on the flow rates, haematocrits and other quantities per vessel, as well as discussions on other considerations with regard to comparing with *in vivo* data, can be found in our previous works (Balogh & Bagchi 2017*b*, 2018).

REFERENCES

ABKARIAN, M., LARTIGUE, C. & VIALLAT, A. 2002 Tank treading and unbinding of deformable vesicles in shear flow: determination of the lift force. *Phys. Rev. Lett.* **88**, 068103.

BALOGH, P. & BAGCHI, P. 2017*a* A computational approach to modeling cellular-scale blood flow in complex geometry. *J. Comput. Phys.* **334**, 280–307.

BALOGH, P. & BAGCHI, P. 2017*b* Direct numerical simulation of cellular-scale blood flow in 3D microvascular networks. *Biophys. J.* **113**, 2815–2826.

BALOGH, P. & BAGCHI, P. 2018 Analysis of red blood cell partitioning at bifurcations in simulated microvascular networks. *Phys. Fluids* **30**, 051902.

BARBEE, K. 2002 Role of subcellular shear-stress distributions in endothelial cell mechanotransduction. *Ann. Biomed. Engng* **30**, 472–482.

BENEDICT, K., COFFIN, G., BARRETT, E. & SKALAK, T. 2011 Hemodynamic systems analysis of capillary network remodeling during the progression of type 2 diabetes. *Microcirculation* **18**, 63–73.

BLOCH, E. 1962 A quantitative study of the hemodynamics in the living microvascular system. *Am. J. Anat.* **110**, 125–154.

BRUST, M., AOUANE, O., THIEBAUD, M., FLORMANN, D., VERDIER, C., KAESTNER, L., LASCHKE, M., SELMI, H., BENYOUSSEF, A., PODGORSKI, T., COUPIER, G., MISBAH, C. & WAGNER, C. 2014 The plasma protein fibrinogen stabilizes clusters of red blood cells in microcapillary flows. *Sci. Rep.* **4**, 4348.

BUGLIARELLO, G. & SEVILLA, J. 1970 Velocity distribution and other characteristics of steady and pulsatile blood flow in fine glass tubes. *Biorheology* **7**, 85–701.

CANTAT, I. & MISBAH, C. 1999 Lift force and dynamical unbinding of adhering vesicles under shear flow. *Phys. Rev. Lett.* **83**, 880–883.

CASSOT, F., LAUWERS, F., FOUARD, C., PROHASKA, S. & LAUWERS-CANCES, V. 2006 A novel three dimensional computer-assisted method for a quantitative study of microvascular networks of the human cerebral cortex. *Microcirculation* **13**, 1–18.

https://doi.org/10.1017/jfm.2019.45 Published online by Cambridge University Press

CHADWICK, R. 1985 Slow viscous flow inside a torus – the resistance of small tortuous blood vessels. *Q. Appl. Maths* **43**, 317–323.

COPLEY, A. & STAPLE, P. 1962 Haemorheological studies on the plasmatic zone in the microcirculation of the cheek pouch of Chinese and Syrian hamsters. *Biorheology* **1**, 3–14.

CROWL, L. & FOGELSON, A. 2010 Computational model of whole blood exhibiting lateral platelet motion induced by red blood cells. *Intl J. Numer. Meth. Biomed. Engng* **26**, 471–487.

COUPIER, G., KAOUI, B., PODGORSKI, T. & MISBAH, C. 2008 Noninertial lateral migration of vesicles in bounded Poiseuille flow. *Phys. Fluids* **20**, 111702.

DAVIES, P. & TRIPATHI, S. 1993 Mechanical stress mechanisms and the cell: an endothelial paradigm. *Circulat. Res.* **72**, 239–245.

ENDEN, G. & POPEL, A. 1994 A numerical study of plasma skimming in small vascular bifurcations. *Trans. ASME J. Biomech. Engng* **116**, 79–88.

FAIVRE, M., ABKARIAN, M., BICKRAJ, K. & STONE, H. 2006 Geometrical focusing of cells in a microfluidic device: an approach to separate blood plasma. *Biorheology* **43**, 147–159.

FEDOSOV, D., CASWELL, B., POPEL, A. & KARNIADAKIS, G. 2010 Blood flow and cell-free layer in microvessels. *Microcirculation* **17**, 615–628.

FEDOSOV, D. & GOMPPER, G. 2014 White blood cell margination in microcirculation. *Soft Matt.* **10**, 2961–2970.

FENTON, B., CARR, R. & COKELET, G. 1985 Nonuniform red cell distribution in 20 to 100 μm bifurcations. *Microvasc. Res.* **29**, 103–126.

FREUND, J. 2007 Leukocyte margination in a model microvessel. *Phys. Fluids* **19**, 023301.

FUNG, Y. C. 1993 *Biomechanics: Mechanical Properties of Living Tissues*, 2nd edn. Springer.

FUNG, Y. C. 1996 *Biomechanics: Circulation*, 2nd edn. Springer.

GRANDCHAMP, X., COUPIER, G., SRIVASTAV, A., MINETTI, C. & PODGORSKI, T. 2013 Lift and down-gradient shear-induced diffusion in red blood cell suspensions. *Phys. Rev. Lett.* **110**, 108101.

KATANOV, D., GOMPPER, G. & FEDOSOV, D. 2015 Microvascular blood flow resistance: role of red blood cell migration and dispersion. *Microvasc. Res.* **99**, 57–66.

KIM, S., KONG, R., POPEL, A., INTAGLIETTA, M. & JOHNSON, P. 2006 A computer-based method for determination of the cell-free layer width in microcirculation. *Microcirculation* **13**, 199–207.

KIM, S., KONG, R., POPEL, A., INTAGLIETTA, M. & JOHNSON, P. 2007 Temporal and spatial variations of cell-free layer width in arterioles. *Am. J. Physiol. Heart Circ. Physiol.* **293**, H1526–H1535.

KIM, S., ONG, P. & JOHNSON, P. 2009*a* Effect of dextran 500 on radial migration of erythrocytes in postcapillary venules at low flow rates. *Mol. Cell. Biomech.* **6** (2), 83–91.

KIM, S., ONG, P., YALCIN, O., INTAGLIETTA, M. & JOHNSON, P. 2009*b* The cell-free layer in microvascular blood flow. *Biorheology* **46**, 181–189.

KOUTSIARIS, A., TACHMITZI, S., BATIS, N., KOTOULA, M., KARABATSAS, C., TSIRONI, E. & CHATZOULIS, D. 2007 Volume flow and wall shear stress quantification in the human conjunctival capillaries and post-capillary venules *in vivo*. *Biorheology* **44**, 375–386.

KUMAR, A. & GRAHAM, M. 2012 Mechanism of margination in confined flows of blood and other multicomponent suspensions. *Phys. Rev. Lett.* **109**, 108102.

KRUGER, T. 2016 Effect of tube diameter and capillary number on platelet margination and near-wall dynamics. *Rheol. Acta.* **55**, 511–521.

LEIGHTON, D. & ACRIVOS, A. 1987 Measurement of shear-induced self-diffusions in concentrated suspensions of spheres. *J. Fluid Mech.* **177**, 109–131.

LIAO, J., HEIN, T., VAUGHN, M., HUANG, K. & KUO, L. 1999 Intravascular flow decreases erythrocyte consumption of nitric oxide. *Proc. Natl Acad. Sci. USA* **96**, 8757–8761.

LIPOWSKY, H., KOVALCHECK, S. & ZWEIFACH, B. 1978 The distribution of blood rheological parameters in the microvasculature of cat mesentery. *Circulat. Res.* **43**, 738–749.

MAEDA, N., SUZUKI, Y., TANAKA, J. & TATEISHI, N. 1996 Erythrocyte flow and elasticity of microvessels evaluated by marginal cell-free layer and flow resistance. *Am. J. Phys.* **271**, H2454–H2461.

https://doi.org/10.1017/jfm.2019.45 Published online by Cambridge University Press

MURATA, S., MIYAKE, Y. & INABA, T. 1976 Laminar flow in a curved pipe with varying curvature. *J. Fluid Mech.* **73**, 735–752.

NAMGUNG, B. & KIM, S. 2014 Effect of uneven red cell influx on formation of cell-free layer in small venules. *Microvasc. Res.* **92**, 19–24.

NAMGUNG, B., ONG, P., JOHNSON, P. & KIM, S. 2011 Effect of cell-free layer variation on arteriolar wall shear stress. *Ann. Biomed. Engng* **39**, 359–366.

NG, Y., NAMGUNG, B., TIEN, S., LEO, H. & KIM, S. 2016 Symmetry recovery of cell-free layer after bifurcations of small arterioles in reduced flow conditions: effect of RBC aggregation. *Am. J. Physiol. Heart Circ. Physiol.* **311**, H487–H497.

ONG, P., JAIN, S. & KIM, S. 2012 Spatio-temporal variations in cell-free layer formation near bifurcations of small arterioles. *Microvasc. Res.* **83**, 118–125.

ONG, P., JAIN, S., NAMGUNG, B., WOO, Y., SAKAI, H., LIM, D., CHUN, K. & KIM, S. 2011 An automated method for cell-free layer width determination in small arterioles. *Physiol. Meas.* **32**, N1–N12.

ONG, P., NAMGUNG, B., JOHNSON, P. & KIM, S. 2010 Effect of erythrocyte aggregation and flow rate on cell-free layer formation in arterioles. *Am. J. Physiol. Heart Circ. Physiol.* **298**, H1870–H1878.

OULAID, O. & ZHANG, J. 2015 Cell-free layer development process in the entrance region of microvessels. *Biomech. Model. Mechanobiol.* **14**, 783–794.

PERKKIO, J. & KESKINEN, R. 1983 Hematocrit reducing in bifurcations due to plasma skimming. *Bull. Math. Biol.* **45**, 41–50.

PRIES, A., LEY, K., CLAASSEN, M. & GAEHTGENS, P. 1989 Red cell distribution at microvascular bifurcations. *Microvasc. Res.* **83**, 81–101.

PRIES, A., SECOMB, T. & GAEHTGENS, P. 1996 Biophysical aspects of blood flow in the microvasculature. *Cardiovasc. Res.* **32**, 654–667.

POZRIKIDIS, C. 2003 *Modeling and Simulation of Capsules and Biological Cells*, 1st edn. Chapman and Hall/CRC.

REES, D., PALMER, R. & MONCADA, S. 1989 Role of endothelium-derived nitric oxide in the regulation of blood pressure. *Proc. Natl Acad. Sci. USA* **86**, 3375–3378.

REINKE, W., GAEHTGENS, P. & JOHNSON, P. 1987 Blood viscosity in small tubes: effect of shear rate, aggregation, and sedimentation. *Am. J. Phys.* **253**, H540–H547.

SECOMB, T. & PRIES, A. 2013 Blood viscosity in microvessels: experiment and theory. *C. R. Phys.* **14**, 470–478.

SECOMB, T. 2017 Blood flow in the microcirculation. *Annu. Rev. Fluid Mech.* **49**, 443–461.

SHARAN, M. & POPEL, A. 2001 A two-phase model for flow of blood in narrow tubes with increased effective viscosity near the wall. *Biorheology* **38**, 415–428.

SINGH, R., LI, X. & SARKAR, K. 2014 Lateral migration of a capsule in plane shear near a wall. *J. Fluid Mech.* **739**, 421–443.

SKALAK, R., TOZEREN, A., ZARDA, P. & CHIEN, S. 1973 Strain energy function of red blood cell membranes. *Biophys. J.* **13**, 245–264.

SMIESKO, V. & JOHNSON, P. 1993 The arterial lumen is controlled by flow-related shear stress. *News Physiol. Sci.* **8**, 34–38.

SOUTANI, M., SUZUKI, Y., TATEISHI, N. & MAEDA, N. 1995 Quantitative evaluation of flow dynamics of erythrocytes in microvessels: influence of erythrocyte aggregation. *Am. J. Phys.* **268**, H1959–H1965.

TATEISHI, N., SUZUKI, Y., SOUTANI, M. & MAEDA, N. 1994 Flow dynamics of erythrocytes in microvessels of isolated rabbit mesentery: cell-free layer and flow resistance. *J. Biomech.* **27**, 1119–1125.

VERKAIK, A., BEULEN, B., BOGAERDS, A., RUTTEN, M. & VAN DE VOSSE, F. 2009 Estimation of volume flow in curved tubes based on analytical and computational analysis of axial velocity profiles. *Phys. Fluids* **21**, 023602.

WANG, C. & BASSINGTHWAIGHTE, J. 2003 Blood flow in small curved tubes. *Trans. ASME J. Biomech. Engng* **125**, 910–913.

https://doi.org/10.1017/jfm.2019.45 Published online by Cambridge University Press

YAN, Z., ACRIVOS, A. & WEINBAUM, S. 1991 Fluid skimming and particle entrainment into a small circular side pore. *J. Fluid. Mech.* **229**, 1–27.

YE, S., JU, M. & KIM, S. 2016 Recovery of cell-free layer and wall shear stress profile symmetry downstream of an arteriolar bifurcation. *Microvasc. Res.* **106**, 14–23.

YIN, X. & ZHANG, J. 2012 Cell-free layer and wall shear stress variation in microvessels. *Biorheol.* **49**, 261–270.

YIN, X., THOMAS, T. & ZHANG, J. 2013 Multiple red blood cell flows through microvascular bifurcations: cell free layer, cell trajectory, and hematocrit separation. *Microvasc. Res.* **89**, 47–56.

ZAKRZEWICZ, A., SECOMB, T. & PRIES, A. 2002 Angioadaptation: keeping the vascular system in shape. *Physiology* **17**, 197–201.

ZHAO, H., SHAQFEH, E. & NARSIMHAN, V. 2012 Shear-induced particle migration and margination in a cellular suspension. *Phys. Fluids* **24**, 011902.

ZONG-CAN, O. & HELFRICH, W. 1989 Bending energy of vesicle membranes: general expressions for the first, second, and third variation of the shape energy and applications to spheres and cylinders. *Phys. Rev.* A **39**, 5280–5288.

https://doi.org/10.1017/jfm.2019.45 Published online by Cambridge University Press